



REPORT OF INVESTIGATIONS 9666
April 2006

APPLICATIONS OF GROUND-BASED RADAR TO MINE SLOPE MONITORING

Edward L. McHugh, Jami Dwyer, David G. Long, and Charles Sabine



Department of Health and Human Services
Centers for Disease Control and Prevention
National Institute for Occupational Safety and Health



Cover: Haul truck passing below a failing slope in a Wyoming coal mine. Note that the arcuate failure surface reaches almost to the top of the slope.

REPORT OF INVESTIGATIONS 9666

**APPLICATIONS OF GROUND-BASED RADAR TO MINE SLOPE
MONITORING**

Edward L. McHugh, Jami Dwyer, David G. Long, and Charles Sabine

**DEPARTMENT OF HEALTH AND HUMAN SERVICES
CENTERS FOR DISEASE CONTROL AND PREVENTION
NATIONAL INSTITUTE FOR OCCUPATIONAL SAFETY AND HEALTH**

April 2006

ORDERING INFORMATION

Copies of National Institute for Occupational Safety and Health (NIOSH) documents and information about occupational safety and health are available from

NIOSH-Publications Dissemination
4676 Columbia Parkway
Cincinnati, OH 45226-1998

FAX: 513-533-8573
Telephone: 1-800-35-NIOSH
e-mail: pubstaft@cdc.gov
Web site: www.cdc.gov/niosh

This document is in the public domain and may be freely copied or reprinted.

Disclaimer:

The findings and conclusions in this paper are those of the authors and do not necessarily represent the views of the National Institute for Occupational Safety and Health (NIOSH), nor does mention of any company or product constitute endorsement by NIOSH.

DHHS (NIOSH) Publication No. 2006-116

TABLE OF CONTENTS

	Page
Abstract	1
Introduction.....	2
Factors limiting slope stability	2
Standard highwall monitoring	2
Displacement monitoring using radar	3
Radar technology	3
History.....	4
Imaging radar interferometry	5
Differential interferometry.....	6
Ground-based differential radar.....	6
Static differential radar	6
SAR interferometry	7
Two-dimensional scanning interferometry	7
Tracking mining hazards with radar	8
Background.....	9
Theory and methods	9
Field experiments	10
Results and analysis.....	12
Conclusions	16
References	21
Appendixes	
A: The science of radar	20
B: Data tables on field experiments using radar to detect mining hazards	27

FIGURES

	Page
1.—Highway failure at stone operation crushed dozer and fatally injured dozer operator.....	3
2.—Geometry of imaging radar system showing azimuth, look direction, and footprint.....	6
3.—Aircraft carrying the YINSAR system.	8
4.—Geometry of a system using two receiving antennas for elevation modeling	10
5.—Two-dimensional scanning radar configuration	10
6.—One-dimensional scanning radar configuration.....	10
7.—Site of YINSAR slope monitoring experiments	11
8.—Radar view of slope with man climbing.	11
9.—Baseline of slope with no displacement, test 1.....	13
10.—Rock thrown onto slope at about 6 sec, test 2.....	13
11.—Man ascending slope, test 3.....	14
12.—Man descending slope, test 4.....	14
13.—Range interferometric phase image from test 4 showing data analysis segments.....	15
14.—Interferometric phase image from 13 to 26 sec (test 4) showing data source for time/displacement analysis.....	16
15.—Displacement on slope at a range of 32 m from radar, test 4.....	16
16.—Phase profiles along range from bottom to top of slope during three intervals, test 4	17
17.—Diagrammatic radar signatures possible for different failure types using two-dimensional radar configuration	17

TABLES

	Page
1.—Radar wavelengths and frequencies used in remote sensing.....	4
2.—Summary statistics for segments of test 4 data	15
B1.—Phase data for a segment of test 4	27
B2.—Range interferometric phase profile data, test 4	32

UNIT OF MEASURE ABBREVIATIONS USED IN THIS REPORT

cm	centimeter	m	meter
db	decibel	MHz	megahertz
GHz	gigahertz	min	minute
hr	hour	mm	millimeter
Hz	hertz	mm/hr	millimeter per hour
kHz	kilohertz	sec	second
km	kilometer		

APPLICATIONS OF GROUND-BASED RADAR TO MINE SLOPE MONITORING

Edward L. McHugh,¹ Jami Dwyer,² David G. Long,³ and Charles Sabine⁴

ABSTRACT

Slope failure accidents were responsible for about 12% of U.S. surface mine fatalities between 1995 and 2003. Small surface movements on a mine highwall may be precursors of failure that, if detected, could provide sufficient warning to enable workers and machinery to be withdrawn to safety. Radar interferometry offers the necessary precision to detect these movements. Radar has some advantages over other methods in its ability to cover large surface areas for true two-dimensional monitoring day and night under almost any weather condition. Radar's active transmit/receive mode of operation provides for more direct sampling than do passive optical methods that depend on solar illumination. Improvements in microprocessor speeds and capacities have led to the development of a number of small, portable, ground-based systems; such systems are now being deployed at several locations around the world. As part of an ongoing study of monitoring technologies, researchers from the National Institute for Occupational Safety and Health and Brigham Young University, Provo, UT, cooperated to assess the feasibility of using interferometric radar to monitor mine slope stability. Field tests of a device incorporating prototype equipment were successful in that small, centimeter-scale displacements on rock slopes were detected.

¹Physical scientist, Spokane Research Laboratory, National Institute for Occupational Safety and Health, Spokane, WA.

²Mining engineer, Spokane Research Laboratory, National Institute for Occupational Safety and Health, Spokane, WA.

³Director, Center for Remote Sensing, Brigham Young University, Provo, UT.

⁴Geopix, Sparks, NV.

INTRODUCTION

Some instability can be expected at any surface mining operation, but the unexpected movement of ground endangers lives and destroys property. Unstable slopes are hazardous for miners who work on or beneath them, and large-scale failures have the potential to cause catastrophic loss of life. Between 1995 and 2003, 42 miners died in slope failure accidents at surface mines in the United States. Rocks falling from highwalls above the victims caused 24 of these deaths. While small rockfalls can cause fatal injuries to workers on foot away from the protection of large machinery, shovel operators and drillers suffered the greatest number of fatalities in massive highwall failures.

A research project was begun at the Spokane Research Laboratory, National Institute for Occupational Safety and Health (NIOSH), to improve recognition of slope stability hazards at surface mines. A principal objective of the project is to improve means for detecting conditions in open-pit mines that could lead to catastrophic slope failure. One approach taken was to assess the application of remote-sensing technologies to mine slope safety. Remote sensing is the science of deriving information about a site by using instruments to collect measurements from a distance without making direct contact with the objects being studied.

Three aspects of remote-sensing technology—hyperspectral imaging, interferometric radar, and photographic image analysis—are being evaluated as tools to help recognize potential hazards at mine sites. These technologies have been developed mainly as airborne or satellite instruments, but their spatial resolution and sampling intervals are not sufficient for addressing local ground control problems in surface mines. Only recently have increased microprocessor speeds, data storage capacities, and signal processing capabilities led to the development of smaller, portable, ground-based systems. Adaptation of these technologies to simplified ground-based instruments could provide a cost-effective means to reduce injuries from catastrophic failure of mine slopes.

This paper summarizes developments in the application of ground-based radar to slope stability monitoring and presents information on NIOSH-sponsored experiments recently completed. Field tests of a hyperspectral imager were conducted to assess its value for improving geologic maps of potentially unstable alteration zones on mine slopes (McHugh and others, 2001). Computerized monitoring methods using images from digital and video cameras are being assessed for application to mine slope surveillance (McHugh and Girard, 2002).

FACTORS LIMITING SLOPE STABILITY

Mine slopes are designed with an engineered factor of safety to control the risk of injury and damage to miners and equipment from rock falls and slope failures. Geologic structures, rock mass properties, and hydrologic conditions are elements to be considered in designing a safe and efficient mining operation. The need to control costs commonly results in pit walls being made as steep as practical to minimize waste removal and surface disturbance, and to maximize ore recovery. However, steeper walls normally mean a greater potential for slope instability.

Blasting practices can be adapted to minimize unnecessary fracturing of the highwall. Groundwater, surface water, and precipitation runoff can be controlled to abate their deleterious effects on stability. Benches and berms are normally used to stop rocks before they can fall far enough to present a significant hazard. Mechanical rockfall catchment systems or secondary supports may be used where feasible to stabilize slopes as needed in particular locations.

However, even carefully designed and constructed slopes may fail (figure 1) because of unidentified geologic structures, unexpected weather conditions, or seismic activity. For this reason, regular examination and systematic monitoring of slopes for early warning signs of failure are the most important means of protecting exposed mine workers.

STANDARD HIGHWALL MONITORING

Conventional modern monitoring methods depend on regular benchmark surveys that commonly use reflecting prisms at specific locations as well as visual inspections. These techniques may be augmented by detailed recording of movement at



Figure 1.—Highwall failure at a stone operation crushed dozer and fatally injured dozer operator (November 13, 2002). (Photograph courtesy of Mine Safety and Health Administration, 2002.)

known problem sites using extensometers, tension-crack monitors, or other instruments. Additional instruments can be used as part of a comprehensive system to register subsurface rock mass displacement, groundwater parameters, and blast vibration levels. Aside from visual inspection, these methods provide displacement information only for a single site, or at best, a discrete number of sites. If the monitored sites are too widely separated or if displacement occurs between sites, early indications of a pending slope failure might go unnoticed. In addition, these monitoring tools are difficult to install at many quarries and surface coal mines where steep highwalls and lack of benches limit access to areas above the working floor. As mining progresses and monitoring different sections of the pit walls becomes necessary, relocating monitoring devices is not only costly and time consuming, but can also be dangerous on unstable slopes.

Point-by-point monitoring of every potential failure block on a mine slope is not practical, but a new generation of scanning laser rangefinders has partially addressed this under-sampling problem by detecting movement over large areas. These instruments can generate digital models of mine slopes without reflector prisms. Displacement can be detected by comparing successive scans. Scanning lasers will likely prove to be a practical solution in some mine slope monitoring applications, but processing requirements and scan rates have so far made repeat pass intervals too great for effective, timely slope monitoring. In addition, the range and accuracy of these systems can be impaired by differences in the reflectivity of the rock, the angle of the rock face, weather, vegetation, and other factors.

DISPLACEMENT MONITORING USING RADAR

Radar has some advantages over other methods in its ability to cover large areas on the surface for true two-dimensional monitoring day and night in almost any weather, and atmospheric dust and/or haze have little effect. Radar's active transmit/receive mode of operation also provides an advantage over passive optical methods that depend on solar or other illumination.

Although radar technology has been widely used for the last 50 years, only in the last 10 years have advancing computer capabilities provided the low-cost processing power needed for interferometric computations. The widespread adoption of modern wireless communication devices has resulted in practical integrated circuits for microwave frequencies that can be used in task-specific radar applications. To evaluate this technology and to assess the feasibility of using interferometric radar to monitor mine slope stability using prototype equipment, a cooperative agreement was established between NIOSH and the Center for Remote Sensing at Brigham Young University (BYU), Provo, UT.

RADAR TECHNOLOGY

The term *radar* is an acronym for Radio Detection and Ranging. It operates in the radio and microwave portions of the electromagnetic spectrum at wavelengths ranging from a few millimeters to about a meter. The radar spectrum is itself divided into a number of *bands* having letter designations that were originally adopted for security reasons during World War II and that are still used as a shorthand reference (table 1). Radar is an *active* remote sensing system that provides its own energy to illuminate targets of interest and records the return signal reflected from a target. *Passive* systems, such as aerial photography and multispectral sensors, detect solar or thermal radiation reflected or radiated from the ground. Because radar systems provide their own energy, they can operate during daylight or at night. Systems with longer wavelengths can penetrate clouds to reveal the terrain beneath.

Table 1.—Radar wavelengths and frequencies used in remote sensing.

Band	Wavelength (λ), cm	Frequency (ν), GHz (10^9 cycles/sec)	Common applications
Ka (0.86 cm)	0.8 to 1.1	40.0 to 26.5	Navigation, weather, synthetic vision, altimeters
K	1.1 to 1.7	26.5 to 18.0	Weather, police, scatterometers, Doppler location
Ku	1.7 to 2.4	18.0 to 12.5	Search, fire control, altimeters, scatterometers, precipitation
X (3.0, 3.2 cm)	2.4 to 3.8	12.5 to 8.0	Navigation, surveillance, SAR, weather, police
C	3.8 to 7.5	8.0 to 4.0	SAR, weather, fire control, altimeters
S	7.5 to 15.0	4.0 to 2.0	Maritime, weather, space, SAR, microwave ovens
L (23.5, 25.0 cm)	15.0 to 30.0	2.0 to 1.0	Early warning, SAR, SEASAT
P	30.0 to 100.0	1.0 to 0.3	Early warning, SAR, wind profilers

Bands with wavelengths in parentheses are those most often used in imaging radars. Letter designations were adopted during World War II for security reasons. (Adapted from U.S. Dept. of Commerce, 2003, and Skolnik, 1990.)

HISTORY

Observers noted the reflection of radio waves from objects in the landscape in the late nineteenth century. The first patent for using radar to detect ships was issued in 1904. Research and development took place in the United States, Britain, and Germany almost simultaneously during the 1920's and 1930's, with the United States and Britain focusing primarily on navigation and detection of aircraft and ships. Significant advances were made in radar development by both Allied and Axis countries during World War II.

Early radar systems utilized the familiar rotating antenna and circular cathode ray tube display known as a *plan position indicator* (PPI). PPI systems transmitting from the ground to the air encountered a great deal of noise or ground clutter. Investigators first tried to eliminate it, but soon realized that the noise was a crude image of the ground terrain. This led to airborne PPI's that directed their signals downward toward the ground to provide a continuously updated "map" of the surface as a navigation aid. Pilots and navigators used boundaries between contrasting surfaces, such as water and land, or large features, such as buildings and cities, to find their way to their destinations.

British night-fighter aircraft first used airborne radar to detect enemy aircraft and later as an aid for nighttime or inclement-weather bombing. This later application led directly to the development of side-looking airborne radar (SLAR) mapping by the military in the early 1950's as a means to acquire images of ground surfaces without flying directly over the imaged area. Data were recorded on photographic film as holograms that were converted to images by a set of optical lenses. These early imaging radars were real-aperture or "brute force" systems. Advances in antenna design, centimeter-wavelength components, and recording devices significantly improved resolution for military reconnaissance.

Declassification of SLAR technology led to an explosion of research and development through the 1960's, and imaging radar soon became a useful remote-sensing tool. Real-aperture surveys became available commercially in 1969. These early systems were simple in design, required little signal processing, and were inexpensive to operate. However, these noncoherent SLAR's could not generate high-resolution imagery from data collected at long range. The National Aeronautics and Space Administration (NASA) acquired extensive unclassified, multi-polarized, K-band imagery of the United States during the late 1960's and early 1970's. Companies such as Westinghouse, Motorola, and Goodyear/Aeroservice actively collected radar data in the United States and other countries, including Panama, Brazil, Venezuela, Nigeria, and Indonesia. Radar's capability to penetrate clouds in tropical regions led to the first detailed maps of these areas.

Synthetic aperture radar (SAR) was being developed concurrently with real-aperture radar in the early 1950's. The concept of SAR is generally attributed to Carl Wiley of the Goodyear Aircraft Corp., who found that an artificially long antenna could be synthesized using a transported small antenna. For a coherent radar system, a Doppler shift from reflected objects occurred as the objects appeared to pass through the radar beam. Spectral analysis of Doppler and phase histories of return signals resulted in constant azimuth resolution as a function of range (Curlander and McDonough, 1991). Resolution of a radar image improves as wavelength becomes shorter with respect to antenna length. Transporting a relatively small antenna to synthesize a long antenna (aperture) permitted the use of longer wavelengths, which are less sensitive to atmospheric attenuation, and the acquisition of fine spatial resolution at high altitudes (Campbell, 1996). Advances in signal-processing techniques over the succeeding decades and the introduction of "chirp" encoding of transmitted pulses led to high-resolution images that could be acquired at long ranges. Imaging radar could now be deployed on orbital platforms.

With the launch of Landsat 1 in 1972, remote-sensing research was directed away from radar toward reflected radiation collected by optical-mechanical scanners in the visible and near-infrared portions of the electromagnetic spectrum. Subsequent launches of Landsat 2 in 1975 and Landsat 3 in 1978 provided repeated worldwide coverage of the earth's surface at a resolution of 80 m.

After almost a decade of data collection by Landsat, limitations in the imaging data had become apparent. Cloud cover was the most serious limitation; vast regions of tropical terrain shrouded in clouds had never been imaged by Landsat. A second limitation was the seasonally restricted solar illumination at high latitudes, particularly during long polar nights. There was a pressing need to monitor sea ice in shipping lanes on a 24-hour basis, which Landsat could not provide.

Radar was recognized as a possible answer to these problems because surface interactions in the microwave portion of the electromagnetic spectrum can provide new information that is different from what is observed in the visible and near-infrared. Oceanographers realized that while color information provided by visible light was important, active radar systems could provide additional information on the state of the sea. Seasat, the first SAR imaging radar in space, was launched in June 1978 to investigate oceanic phenomena, such as ocean roughness, wave patterns, currents, and pack ice. However, it shut down prematurely in October 1978 because of an electrical failure. In the few months it was operational, Seasat proved valuable for terrestrial observations as well, despite its small incidence angle that caused severe distortions in mountainous areas. Geoscientists found a wealth of structural and geomorphic information in Seasat images that led to renewed interest in imaging radar. Seasat was followed by space shuttle imaging radar experiments (SIR-A, SIR-B) and a host of follow-on commercial and research radar satellites still currently in operation (Richards and Jia, 1999).

IMAGING RADAR INTERFEROMETRY

Radar interferometry is the use of radar signals traveling two different paths to determine range information from the coherent interference between the two signals. Imaging radar interferometry combines images recorded from antennas at two different locations to form a spatial baseline. Using the phase difference between the returns to the antennas, interferograms can be constructed that record minute differences on a subwavelength scale for corresponding points on the image pair. Such interferograms can be used to map topography, measure velocities of objects, and detect temporal change. An important application of interferometry in radar is topographic mapping (Zebker and others, 1992; Robertson, 1998; Thompson, 2001) where interferometry is combined with SAR to make radar backscatter images and to derive surface topography.

Spatial baselines are used primarily for topographic mapping. A basic SAR configuration is employed with the beam orthogonal to the track. Two receiving antennas are used, usually with one mounted over the other on the fuselage of an aircraft or on a satellite. This sort of configuration allows measurement of target height relative to the platform to subwavelength accuracy. Simultaneous measurement of short range, look direction, and look angle provides absolute three-dimensional locations of each image point (figure 2). From these data, topographic maps or digital elevation models can be created, and image artifacts such as foreshortening and layover can be corrected.

Topographic mapping can be done with two separate passes and a single receiving antenna or with a single pass and two receiving antennas separated by a fixed baseline in the cross-track (range) direction. In two-pass interferometry, the baseline is defined by the slight difference in the flight paths (in the cross-track direction) of the two passes and requires very precise flight path information. Aircraft interferometers are generally dual-antenna, single-pass systems, while dual-pass interferom-

etry is generally reserved for spacecraft where prediction of the platform's motion is more precise.

Differential Interferometry

Temporal baselines are used for velocity mapping and change detection. Differential interferometry compares interferometric measurements taken at different times to identify very small changes, often smaller than the radar wavelength. The method assumes that measurements are made from identical tracks at different times, which is possible with orbital platforms, but difficult with aircraft. Aircraft motion due to wind drift, roll, pitch, and yaw must be known accurately through precise navigation.

Repeat observations by satellites can record velocities as small as centimeters per day, which is suitable for mapping ice movement and certain kinds of downslope movement. Repeat observation can also be used for longer-term changes of landscape features. If the topography is known, then surface movement due to earthquakes and landslides can be measured, and growth of vegetation can be monitored.

Interferometry can also be used to measure ocean surface currents from moving aircraft by aligning the two antennas in the along-track (azimuth), rather than the cross-track, direction. In this case, interferometry allows estimation of the Doppler shift induced by the moving ocean surface. Azimuth interferometry is sensitive to surface changes in the along-track/vertical plane. An aircraft configured with one antenna behind the other can measure temporal changes on the order of 0.01 to 0.1 sec, which is suitable for measuring velocities on the surface on the order of centimeters per second. This type of configuration may be used to monitor ocean surface motion and vehicular traffic.

One of the earliest and most spectacular applications of radar interferometry for change detection was accomplished at the site of the Landers earthquake of 1992 in the Mojave Desert of California (Massonnet, 1997; Massonnet and others, 1993, 1994). A sequence of ERS-1 radar satellite images of the Landers area before and after the earthquake revealed interference fringes when topographic effects were removed by means of a digital elevation model. Each cycle of interference fringes corresponded to 28 mm of seismic movement. Interference patterns also revealed movement on smaller faults in the region, including 7 mm of movement on a fault 100 km from the epicenter of the Landers quake. Similar applications of radar satellite data have been used to map and monitor landslides, ice movement, and volcano deformation (Fruneau and Achache, 1996), and subsidence caused by the extraction of groundwater, oil and gas, or minerals (Carnec and others, 1996a, b; Stow, 1996; Dixon, 1995). These pioneering studies have generated enormous interest in the earth sciences community because they point to an entirely new way to study the surface of the Earth.

Ground-Based Differential Radar

Slope-monitoring radar to detect hazards needs a much shorter repeat time and greater spatial resolution than airborne and satellite systems can provide. Ground-based interferometric radar systems have been designed to monitor displacement of unstable slopes both in landslide-prone natural settings and at mine sites.

Static Differential Radar

In 1997, field experiments using a static differential radar configuration were conducted by Malassingne and others (2001) to test its potential for use in monitoring active volcanoes. The system used a wide-band radar centered at 26 GHz (25 to 27 GHz). Short pulses of a few centimeters were transmitted, and return signals were processed to retain phase data. Corner reflectors provide a much stronger back-scatter signal than natural surfaces and, with reflectors, absolute distance can be measured to an accuracy of about 1 mm at a range of 1,500 m. Differential measurements at that range had a typical accuracy of 0.1 mm. Atmospheric effects were almost completely removed by comparing return signals from two locations

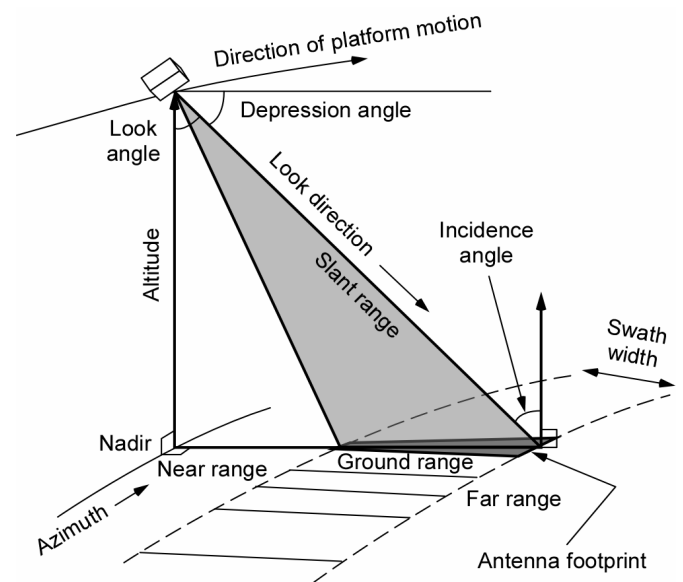


Figure 2.—Geometry of imaging radar system showing azimuth, look direction, and footprint.

separated by a short distance along the line of sight.

Back-scattered responses from natural slopes were used to calculate intercorrelation, from which apparent radial displacement could be measured, to monitor sites that were too unstable for the installation of reflectors or where reflectors had been destroyed. To measure topographic changes, return signals were compared for data collected before and after an interval of time. Decorrelation between the two data sets was a measure of the change that occurred during the interval.

The 1997 field experiments compared a 40- by 40-m active rockfall area to a relatively stable bedrock slope. The targets were sampled in differential mode at a distance of 1 km from the radar antenna and separated by 40 m along the line of sight. The rockfall area showed a substantial decorrelation over the 4 days of the experiment, while the more stable slope where changes were minimal showed a high degree of correlation.

SAR Interferometry

Experiments in the use of ground-based SAR interferometry to detect displacement associated with landslide motion were conducted by Tarchi and others (2003). The site of the experiments was the Tessina earth slide in the eastern Italian Alps. The radar system, called Linear SAR (LISA), consists of continuous-wave stepped-frequency (CW-SF) radar with rail-mounted transmitting and receiving antennas. The survey system, as well as other sensors, serves as an early-warning system for the safety of residential areas below the slide area.

The instruments were mounted at a stable location facing the landslide area at an average distance of 500 m. The radar's field of view is about 800 m long and 350 m wide. The rail was mounted on a concrete wall, and electronic components were installed in an existing building that also contained robotic survey instruments used to monitor the position of 30 benchmarks on the slope automatically.

The radar operated in the frequency band of 16.70 to 16.78 GHz with steps of 100 kHz for a total of 801 frequency points. The synthetic antenna aperture was attained by moving the antennas along a straight rail across 2.4 m at 6-mm steps for a total of 401 azimuth points. Acquisition time was about 14 min. The radar system configuration and slope geometry resulted in a range resolution of about 2 m and an azimuth resolution of about 2 m at the center of the range. Differential interferometry for the system had a theoretical displacement resolution of about 0.5 mm along the radar line of sight, equivalent to a phase shift of about 20° at the frequencies used.

Repeat pass (zero baseline) data collection over a period of several days yielded data sets to produce about 400 SAR images. Pairs of images were used to generate differential interferograms showing displacement over time on the landslide surface. Unwrapping the phase shift through successive interferograms over a period of 48 hours yielded a nearly constant 11.7 mm/hr rate of displacement at one surveyed benchmark. This displacement agreed to within 3 mm with surveyed data over the interval.

Because the design allows for short repeat times (about four times an hour), changes in dielectric constants are negligible. A mask is applied to eliminate pixels where temporal decorrelation has diminished the reliability of the phase measurement. The experiments showed that this approach to slope monitoring can produce highly accurate displacement information over virtually the entire slope with a 2-m spatial resolution.

Two-Dimensional Scanning Interferometry

A scanning radar system using differential interferometry was designed by researchers at the University of Queensland, Australia (2002) specifically for monitoring mine slopes. The system, known as slope stability radar (SSR), uses real-aperture, 2° beam-width radar to scan a slope both vertically (height) and horizontally (azimuth). Scanning at a rate of $10^\circ/\text{sec}$ over a range of $\pm 60^\circ$ vertically and 340° horizontally, the system continuously monitors the slope face for deformation. The return signal phase is recorded for each pixel in the resulting image, and phase unwrapping is used to remove the 2π ambiguity (Reeves and others, 1997, p. 123).

A commercial trailer-mounted unit is available for lease (Ground Probe Pty., Ltd., S. Brisbane, Australia). It features a 0.92-m-diameter scanning parabolic dish antenna, mounts, controlling/data-collecting computer, remote area power supply,

warning siren and lights, CCD camera, communication links, and Internet compatibility. Typical scan repeat time is 15 min. The system can operate at a range up to 450 m from the target slope. Line-of-sight displacement can be measured to ± 0.2 mm without the use of reflectors.

In operation, the system produces an image that shows spatial deformation relative to a reference image for the entire slope scanned. The displacement history of each point in the image can be plotted. Total displacements and rates of change on the slope are valuable factors in assessing the risk to operations below and when or if operations should be discontinued.

TRACKING MINING HAZARDS WITH RADAR

A radar system designed and assembled at BYU was configured for a series of experiments to evaluate the approach for identifying small-scale displacement on mine slopes. The technology stems from research efforts at BYU to build a low-cost interferometric synthetic-aperture radar (InSAR) system that could be deployed in light aircraft and operate at low altitudes (Lundgreen and others, 2000). NIOSH funding facilitated field tests of a ground-based version of the radar system to detect and measure displacement on mine slopes. Such displacement measurements can be used to track mass movement of failing slopes in surface mines and possibly warn of imminent catastrophic collapse. The ground-based approach has the distinct advantages of high resolution derived from a smaller radar footprint and a high sampling rate (repeat times in seconds) to provide real-time displacement detection.

The compact InSAR developed at BYU's Center for Remote Sensing is intended to make imaging radar inexpensive enough for small-scale mapping projects (figure 3). The system was funded in part by a NASA grant (Thompson and others, 1998) and has been used recently in collaboration with the U.S. Geological Survey to periodically collect images of a landslide area in Colorado.



Figure 3.—Aircraft carrying the InSAR system. Insert shows computer and IF/RF subsystems, and laptop controller.

BACKGROUND

After developing a series of small, low-cost SAR systems in the mid-1990's, the design team at BYU began development of a novel, non-SAR interferometric radar system designed to detect railroad track hazards resulting from rockfalls. This system was designed to be very low cost and short range (Waite, 2000). The intention was to adapt this system (by extending its range) to support experiments in highwall stability monitoring. As the track hazards system developed, the design proved to have inadequate long-term phase stability and could not be used for the proposed mine slope experiments. As a result, development was initiated for a new prototype natural hazards radar system with an improved chirp transmitter and a fully coherent oscillator scheme to maximize long-term stability. The original system has since been modified by an independent firm for use as a road traffic monitoring system and is now being sold commercially.

At the same time, development was begun of an X-band interferometric SAR system (known as YINSAR) for operation in a small plane (figure 3). When completed, the YINSAR system was successfully used in a multi-season experiment to collect interferometric data over a landslide in Colorado and an archeology site in Utah. Conclusion of the planned flight program allowed a reconfiguration of the YINSAR hardware to support the mine slope monitoring experiments.

THEORY AND METHODS

Experiments were designed to demonstrate that changes in an interferometric radar signal resulting from small changes in a rock face could be detected in a mine environment. Interferometry is based on the difference in signal phase between two observations and thus requires a coherent (phase-preserving) measurement system. Interferometry is widely used in radio astronomy and has become important in radar where the inherent coherence of radar signals can be exploited. With YINSAR, two antennas separated by a baseline receive a radar echo from a target surface. The antennas are offset in the cross-track (range) direction. The phase difference in the echo from each distance (range) bin measured at each antenna can be related via the geometry of the measurement to the height of the surface (Zebker and Goldstein, 1986).

Small surface movements on a mine highwall that could be precursors to a failure may provide sufficient warning to enable men and machinery to be withdrawn to safety (Fukuzono, 1990; Voight, 1989). Such movements may be less than a few centimeters and thus require precision measurement systems. Radar interferometry offers the desired precision and can operate at night and through smoke and dust without requiring reflectors on a highwall face. This feature allows workers to avoid the hazards they would face while installing reflectors on a potentially unstable highwall.

In simple terms, radar measures the path length between the antennas and each resolved portion of the highwall face. Changes in the path length will be due to movement on the highwall face. As suggested by the geometry shown in figure 4, cross-track interferometry compares distance to the target from each antenna by tracking relative phases of the return signal at each antenna to yield height information in the cross-track/vertical plane according to the formulas

$$R_1 = \sqrt{(H - h)^2 + x^2}, \quad (1)$$

$$R_2 = \sqrt{(H + B - h)^2 + x^2}, \quad (2)$$

$$\text{and } \Delta R = R_2 - R_1 \quad (3)$$

where R_1 and R_2 = range from target to receiving antennas 1 and 2,
 H = height of lower receiving antenna above datum,
 h = height of target above datum,
 x = horizontal distance to target,
 B = distance between receiving antennas,
 and ΔR = difference in range between target and receiving antennas 1 and 2.

This simple picture is complicated by a number of factors. Humidity variations in the intervening atmosphere can give rise to apparent path length changes. Any variations in the location of the microwave scattering centers within the resolution element due to moisture content, freezing, liquid water, snow, etc., can also give rise to path length changes. These effects vary with radar operating frequency and configuration. While variation of the microwave scattering center with environ-

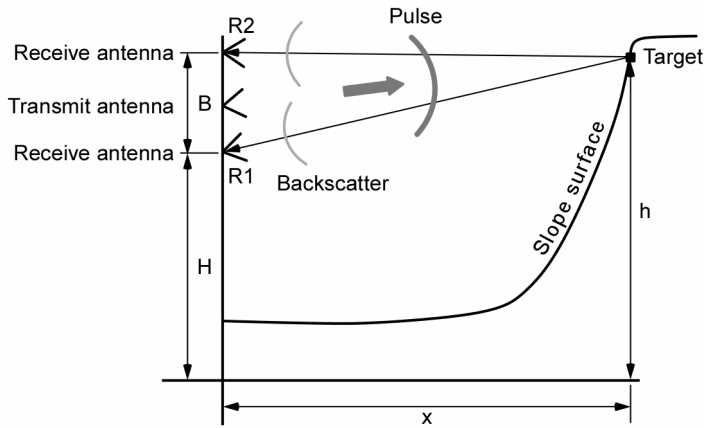


Figure 4.—Geometry of a system using two receiving antennas for elevation modeling.

At each scan location, a radar signal is transmitted, and the radar echo received and processed. The radar signal phase recorded at each scan location is preserved. The face is repeatedly scanned in time. The phase measured at each location is compared to the phase of the previous scan (or a time average of previous scans). Differences in phase between scans are related to face movement with an estimated correction based on weather conditions. This approach requires a high-precision, two-dimensional scanning system and exceptionally phase-stable radar, both conditions that add to the expense of the system. This approach forms the basis of the monitoring system developed in Australia (University of Queensland, 2002).

The second approach adopted for these experiments uses a fan-beam transmitting antenna to illuminate the entire vertical face over a narrow horizontal distance. The face is scanned repeatedly in a horizontal (one-dimensional) sweep (figure 6). Two receiving antennas are separated by a short baseline. The radar's range resolution enables vertical resolution of the face. The interferometric phase difference between the receiving antennas (which is due to the small path length difference between the target and each antenna) is recorded for each scan position. Since the radar is stationary, the differential interferometric phase between scans can be easily computed. The differential phase is very sensitive to changes in the surface in the plane of the baseline orientation, e.g., either azimuth (horizontal) or range (vertical). (Note that with three receiving antennas, azimuth and range interferometry can be done simultaneously.) However, because the interferometric path length for a given scan is nearly the same, the atmospheric effects are similar for both channels, and interference is minimized. Furthermore, this approach does not have the stringent long-term phase stability requirements of the pencil-beam, two-dimensional scan design, although two receivers and antennas are required. In addition, since scanning is in a single dimension, the scanning system is simpler than a two-dimension system.

FIELD EXPERIMENTS

Slope monitoring experiments using the YINSAR apparatus were conducted at a sand-and-gravel operation near Provo, UT (figure 7). To simplify the tests, the system used fixed antenna positions without the scanning configuration necessary to cover the full face as would be required in an operational system. Due to battery power limitations and because the YINSAR hardware is unsuited for long-term outdoor deployment, data were collected only for short periods.

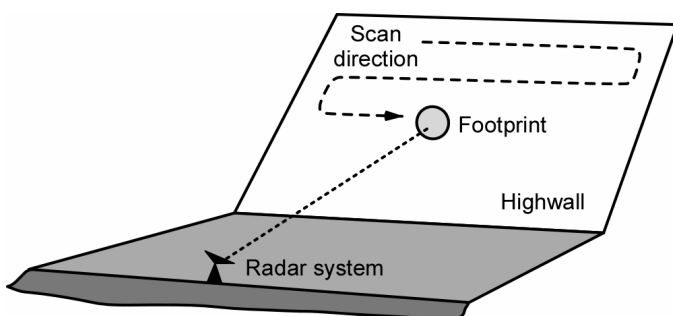


Figure 5.—Two-dimensional scanning radar configuration.

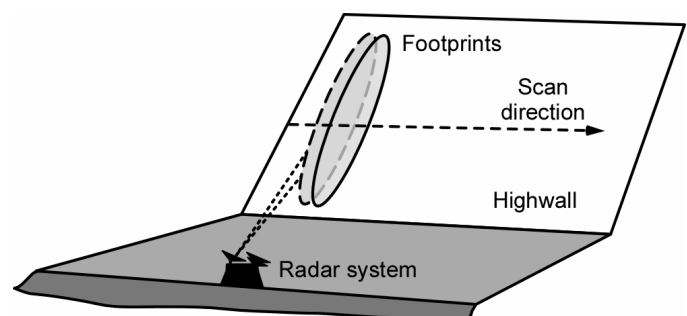


Figure 6.—One-dimensional scanning radar configuration.

mental conditions is inherent to the problem, the effect can be ameliorated by interferometric processing and the operating frequency employed.

Two approaches to the application of radar interferometry for highwall monitoring can be distinguished based on the number, characteristics, and movement of the radar antennas. One approach uses a single, two-dimensional scanning antenna; the second uses dual receiving antennas and one-dimensional scanning. The latter can be further separated into azimuth and range subclasses based on the relative orientation of the two antennas. Both approaches have advantages and disadvantages.

In the first approach, a single pencil-beam antenna is scanned in two dimensions over the highwall face (figure 5).

The system operates at 9.9 GHz with a 200-MHz bandwidth, giving it a 60-cm range resolution. While a lower operating frequency would make the system less sensitive to environment-induced scattering center variations, the system was suitable for a proof-of-concept experiment. The final intermediate frequency is all-digital with the signal digitized at 500 MHz. The pulse repetition frequency was 1200 Hz while the pulse length varied from 0.1 to 150 microseconds.

The system had separate receiving and transmitting antennas (bistatic). The antennas were slotted wave-guide-fed horns with beam widths of approximately 12° horizontally and 45° vertically. The two receiving antennas were in a range interferometric layout with a vertical separation (baseline) of 60 cm (figure 8). A phase change of 2π radians corresponded to 3 cm of surface change. The instrument was set up approximately 30 m from the base of a 35° -gravel slope about 11 m high. Test 1 (baseline) was an initial measurement of the undisturbed slope. Test 2 showed the effect of throwing a softball-sized rock onto the slope, disturbing the surface and shifting a few other rocks. In test 3, a man climbed up the slope, and in test 4, the man descended.



Figure 7.—Site of YINSAR slope monitoring experiments. Gravel pile is about 11 m high and has a slope of about 35° .



Figure 8.—Radar view of slope with man climbing. Inset shows transmitting antenna (left highlight) and receiving antennas (right highlights).

RESULTS AND ANALYSIS

Processed radar data for the four tests are shown in figures 9 through 12. Magnitude and phase are shown graphically for each of the two receiving channels as a function of slant range (distance from the radar) and time. The bottom diagram in each figure combines data from the two channels to show the interferometric phase at each range cell as a function of time. The radar was not scanned as it would be if the entire slope were to be monitored; the images represent a topographic slice along the radar beam from the bottom of the slope to the top over the footprint width of the beam (about 4 m). In figure 9, the vertical band near 0 m is the result of the radar interacting with itself, the ground, and the truck; this can be ignored. The band between 20 and 30 m is the face of the gravel slope. Note that in the later figures, the radar self-interaction occurs at about 10 m, and the slope face is between 30 and 40 m as a result of a change in radar settings.

In the baseline interferometric image (figure 9, bottom), the slope is unchanged over the time of the scan, as shown by the uniform vertical bands (with minor phase variations)—elapsed time runs from 0 sec at the top of the image to more than 9 sec near the bottom. The bands represent the static topography of the slope, as shown by phase differences that result from the different path lengths for return signals to the two vertically separated receiving antennas. The phase values here are unimportant, but result from interaction of radar frequency and the angle of the slope across the range bins.

Figure 10 shows the radar response of a softball-sized rock striking halfway up the slope at about 6 sec. The static profiles of the slope before and after the impact demonstrate the sensitivity of the radar to even very small changes in the surface. The difference in the profiles shows that a lasting change occurred on the slope.

Figure 11 shows the progress of a man climbing the slope as the change in phase moves from nearer to greater range, i.e., from the left of the slope bands near the top of the image diagonally toward the right over a period of less than 20 sec. Figure 12 shows the man descending the slope and the phase change moving closer to the instrument (right to left diagonally) with time. Note the difference in static slope profiles, which reveal surface change before (e.g., 5 sec) and after his passage (30 sec).

A closer look at the interferometric phase plot for data shown in figure 12 provides a method for measuring displacement detected during the test (figure 13). The value of the interferometric phase is shown in the scale at the right of figure 13, extending between approximately $-\pi$ and $+\pi$ radians and encompassing the range of gray-scale color values from 0 to 255. Each pixel in the image array has x and y coordinates and an associated data value (D_v) corresponding to this scale. Image processing software (Envi 3.2) from Research Systems, Inc., Boulder, CO,⁵ was used to quantify the phase scale and radar return data by resolving numeric values pixel by pixel. For the interferometric phase at 0 radians, $D_v = 127$ at the middle of the color range. Lighter colors (higher D_v) have a limit of $D_v = 255$ at a positive interferometric phase of $+\pi$ radians; darker colors (lower D_v) represent a negative phase to $D_v = 0$ at $-\pi$ radians. A D_v change of 41 ($255 - 127/\pi$) therefore represents a phase change of one radian, yielding the following relationships:

$$\Phi = (D_v - 127)/41 \quad (4)$$

and
$$\Delta\Phi = \Delta D_v/41 \quad (5)$$

where Φ = phase, radians,
and $\Delta\Phi$ = phase change, radians.

Phase data are plotted by range in horizontal bands every 0.05 sec down the image (y-axis). Range values (x-axis) are grouped in segments averaging 4.3 pixels wide, corresponding to the 60-cm instrument resolution.

A section of the radar image (box in figure 13) was enlarged to analyze incremental displacement on the slope. For the column of data at 32 m (vertical line in figure 14), D_v was recorded over the interval from 13 to 26 sec, and the difference between each succeeding pixel, sampled at 0.05 sec, was computed. This difference represents the interferometric phase change over the sample increment. The raw data are provided in table B1.

⁵ Mention of specific products and manufacturers does not constitute endorsement by the National Institute for Occupational Safety and Health.

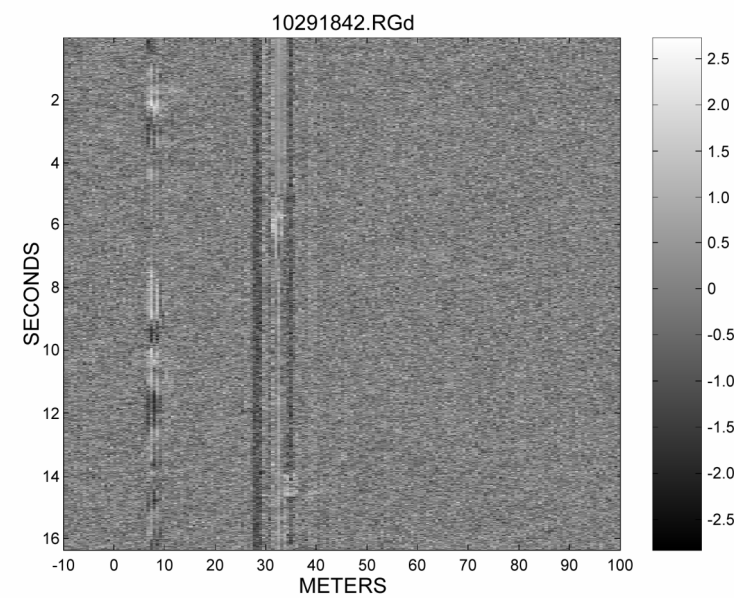
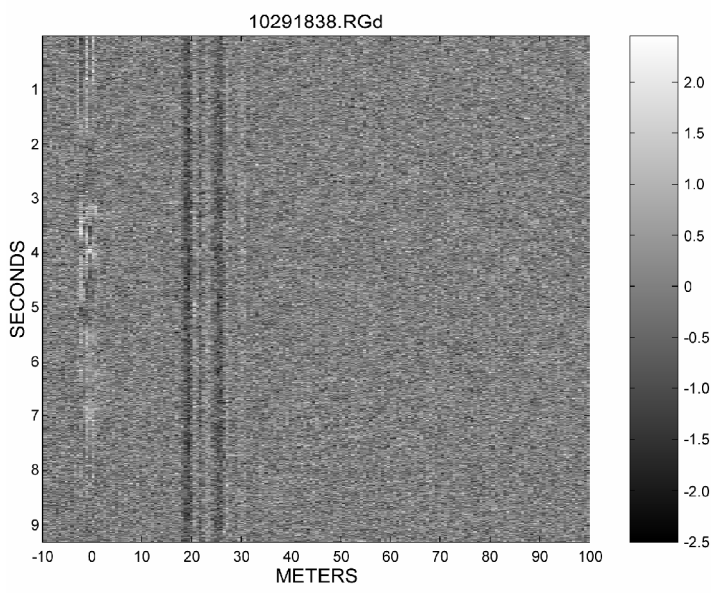
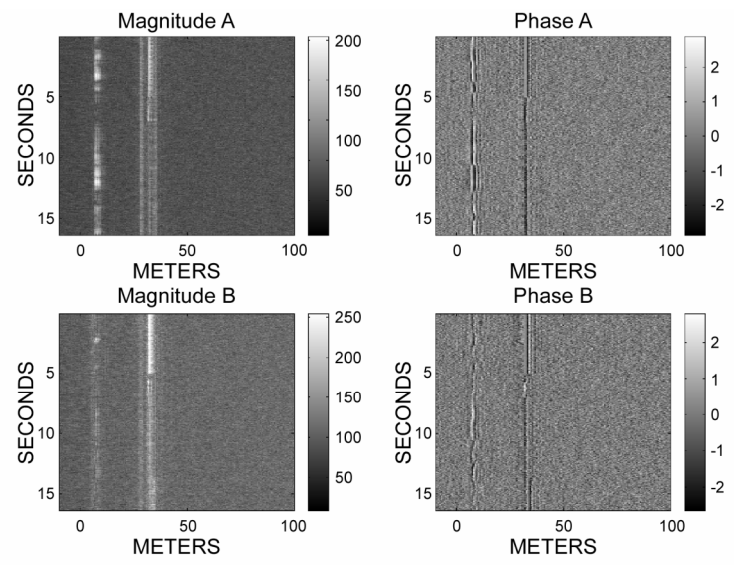
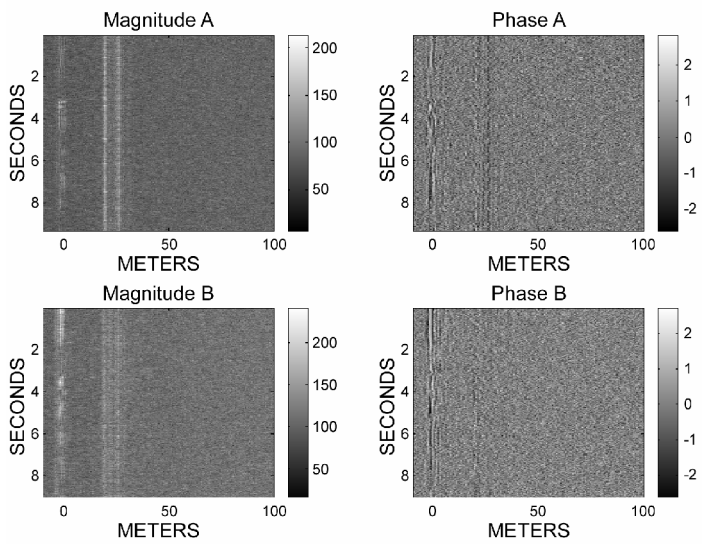


Figure 9.—Baseline of slope with no displacement, test 1. *Top*: Magnitude and phase of each receiving channel as a function of time; *bottom*: range interferometric phase showing self-interference near 0 m and return from slope at about 20 to 30 m.

Figure 10.—Rock thrown onto slope at about 6 sec, test 2. *Top*: Phase of each receiving channel; *bottom*: interferometric phase.

For interferometric radar with separate transmitting and receiving antennas, displacement is related to phase change by the formula—

$$\Delta d = (\Delta\Phi \lambda)/2\pi \tag{6}$$

where Δd = displacement, cm,
 $\Delta\Phi$ = phase change, radians,
 and λ = radar wavelength, cm.

Wavelength of the 9.9-GHz YINSAR radar is 3.03 cm. Displacement that occurred from one time increment to the next is computed by converting the D_v difference between pixels to phase change, then using the above formula. For example, between 18.30 and 18.35 sec, D_v changed from 177 to 9 ($\Delta D_v = -168$), corresponding to a phase difference of -4.10 radians. From the equation, net displacement between those two pixels is $\Delta d = (-4.10 * 3.03)/2\pi$ or $\Delta d = -1.98$ cm. Negative displacement denotes movement toward the instrument (downslope).

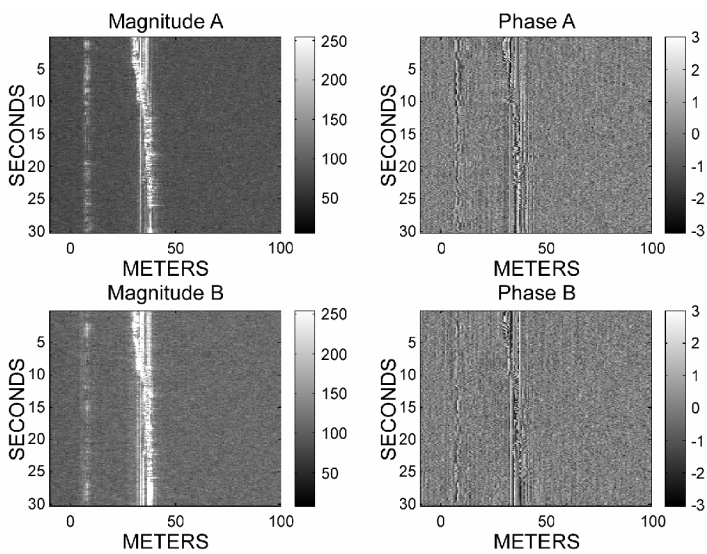


Figure 11.—Man ascending slope, test 3. *Top*: Magnitude and phase of each receiving channel; *bottom*: range interferometric phase.

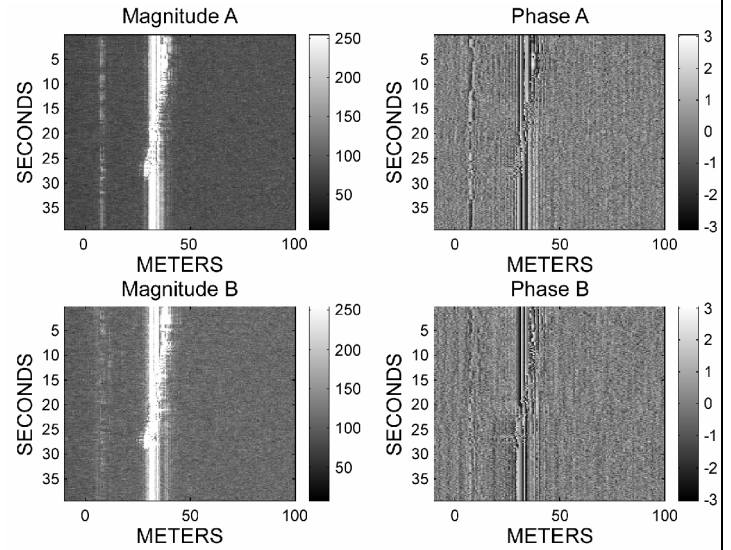


Figure 12.—Man descending slope, test 4. *Top*: Magnitude and phase of each receiving channel; *bottom*: range interferometric phase.

The radar's phase change represents a weighted average of displacements over the footprint of the beam resolution element, representing a net effective displacement. Since the return for a small area within the resolution element is dominated by the background area, we cannot "see" the small area very well, even if the amount of displacement is large. Because we are seeking to detect changes in the average phase for each resolution element over time, detailed phase unwrapping is unnecessary.

Apparent displacement for each successive time increment along the sample line is shown in figure 15. The trace clearly shows an inactive interval prior to the slope disturbance (before), a period of change while the man descends the slope (during), and a restabilization of the slope following the traverse (after). Table 2 provides summary statistics for these intervals. Baseline data show that the system configuration tested has about a 0.2-cm displacement resolution (two standard deviations above the mean) and a signal-to-noise ratio (variance) of 128. The 3-cm maximum possible displacement recorded by this method is determined by the radar wavelength. Measuring cumulative displacement across multiple time increments in this simple experiment was not possible because of inherent phase ambiguity in the data for this particular setup.

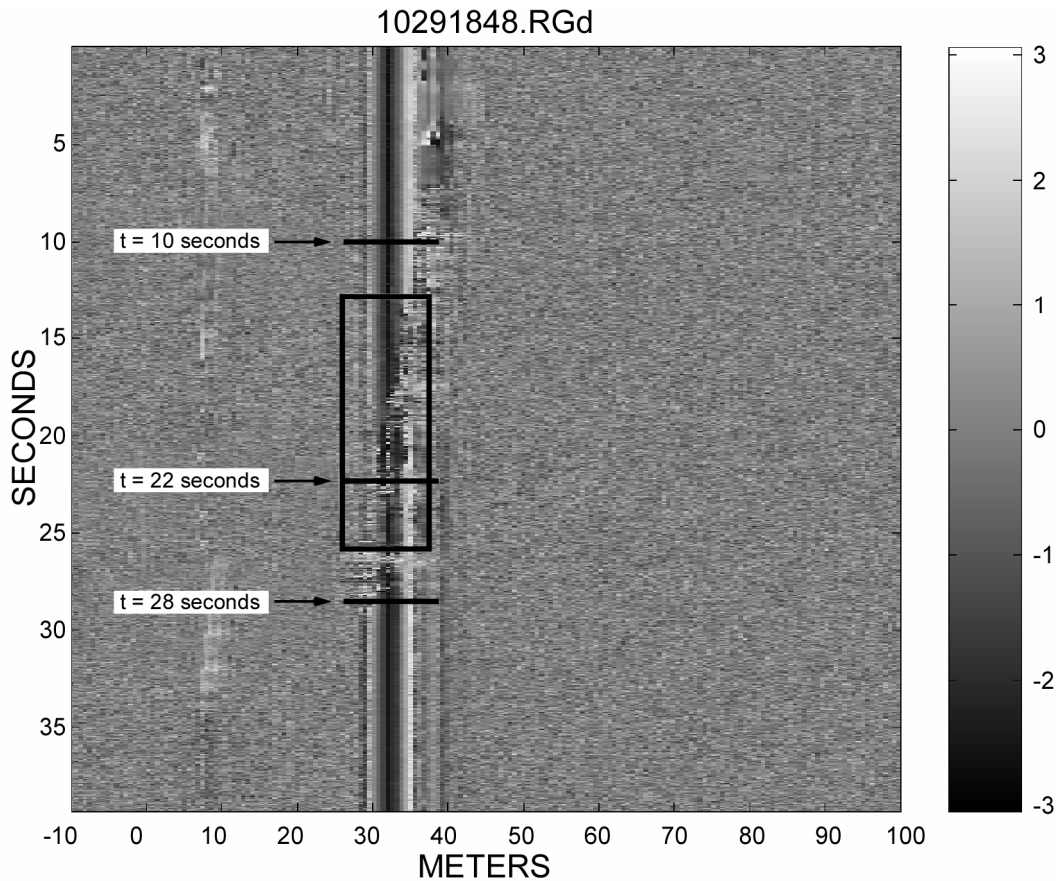


Figure 13.—Range interferometric phase image from test 4 showing data analysis segments.

Table 2.—Summary statistics for segments of test 4 data.

Test segment	Baseline prior to displacement (before)	Active displacement (during)	Stabilizing in new configuration (after)
Time interval, sec	13.0 thru 17.45	17.50 thru 23.14	23.78 thru 25.59
Minimum, cm	-0.56841	-2.59195	-0.23873
Maximum, cm	0.30694	2.56922	0.32968
Range, cm	0.87535	5.16117	0.56841
Sample variance, cm	0.01120	1.43829	0.01914
Standard deviation, cm	0.10585	1.19929	0.13834
Count	83	107	35

Phase data in the range direction allowed the slope profiles to be compared during the test interval. The phase at each range increment from about 26 to 40 m was computed from Dv for 0.1-sec intervals at about times $t = 10, 22,$ and 28 sec (before, during, and after) the man traversed the slope (see figure 13). The results of the analysis are shown in figure 16 (see table B2). The "before" and "after" data show similar profiles, which can be thought of as baseline data; differences reflect a lasting change in slope geometry caused by the man's passage. The "during" data show distinct interferometric phase shifts compared to baseline profiles as a result of active displacement in the radar footprint.

Implementation of a scanning mechanism for horizontal sweeps of the slope with a fan-shaped beam would provide three-dimensional data to assess the stability of the mine highwall. Processing would allow automated computation of displacement, velocities, and acceleration for each point on the slope. Data could be used to generate two-dimensional images of the highwall, such as the examples shown diagrammatically in figure 17, to assist in analyzing failure mechanisms. Using the same scale as in previous interferometric images (e.g., figure 13), where darker colors indicate movement toward the instrument, lighter colors indicate movement away from the instrument, and gray shows no relative

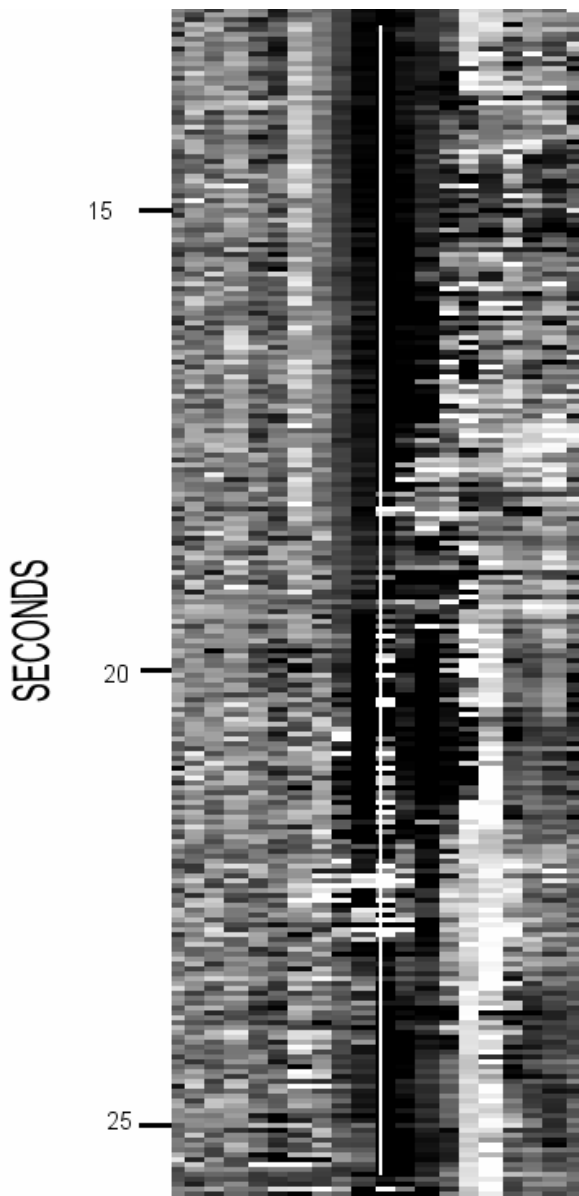


Figure 14.—Interferometric phase image from 13 to 26 sec (test 4) showing data source for time/displacement analysis (vertical line).

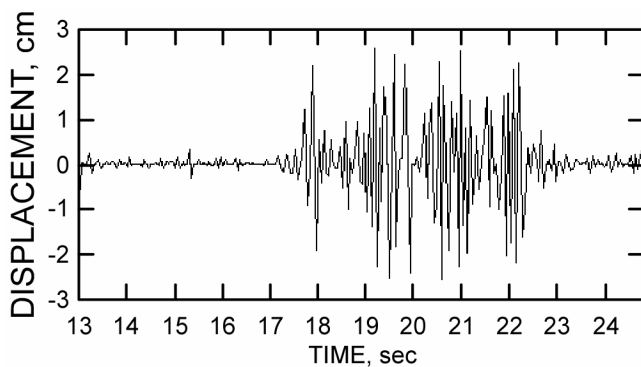


Figure 15.—Displacement on slope at a range of 32 m from radar, test 4.

motion, a scanning system could help define the nature of movement on a slope. Rotational failure is shown by motion both toward and away from the instrument, while wedge and toppling failures are characteristically shown by movement toward the instrument.

CONCLUSIONS

Ground-based interferometric radar has the potential to measure displacement over large areas of mine highwalls at an unprecedented resolution. Prototype versions based on technology from a number of approaches have been introduced at several locations. Based on our simple experiments, range interferometry clearly has the desired sensitivity and thus is a functional approach for low-cost slope monitoring. Further development is required, however.

The objectives for this future work will be to design a practical ground-based interferometric radar instrument for measuring small increments of displacement on rock slopes as an aid to an assessment of slope stability. Such an instrument would be—

- Robust and easily transportable.
- Simple enough to be operated by nonexperts.
- Reasonably priced.
- Able to present displacement data with two- or three-dimensional images of a slope.
- Capable of operating autonomously where continuous monitoring is required.
- Able to measure displacement of less than 1 cm.
- Capable of a spatial resolution approaching 2 m.
- Able to monitor rock slopes from a range of at least 1 km.

Design development to support longer-term experiments will need to address such issues as scanning rates, alarm detection thresholds, the effects of weather, and methods to prevent interference from ordinary mining operations (e.g., movement of equipment). In particular, the effects of weather on radar return from the surface are critical. Moisture on a rock face will likely change the scattering center, which could be interpreted as changes on the monitored slope. Detection algorithms must be sufficiently sophisticated to provide reliable discrimination between changes in atmospheric conditions versus actual displacement. The radar's long-term phase stability and effects of conditions such as snow and ice accumulation on benches or water running down the highwall face need to be tested. Carefully conducted monitoring of real highwall faces with independently verified readings will be essential for ultimately validating this technology.

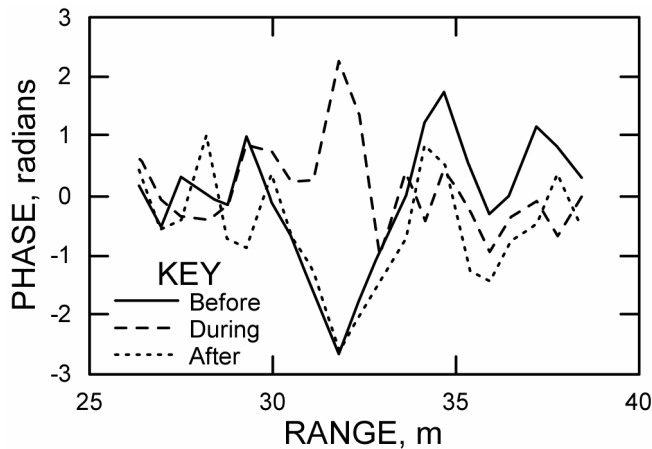


Figure 16.—Phase profiles along range from bottom to top of slope during three intervals, test 4.

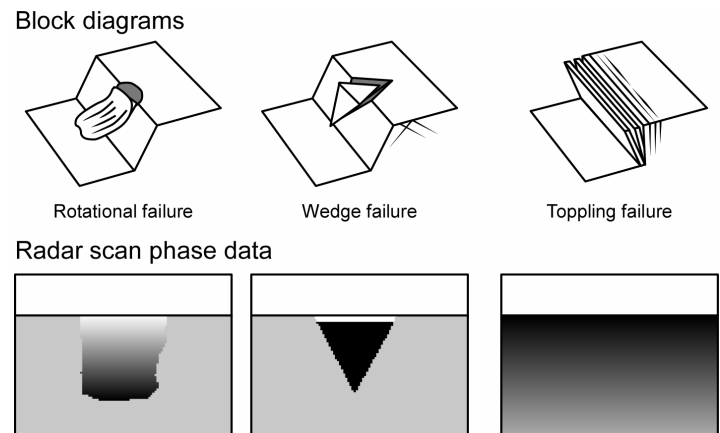


Figure 17.—Diagrammatic radar signatures possible for different failure types using two-dimensional radar configuration.

REFERENCES

- Campbell, J.B. 1996. *Introduction to Remote Sensing*. Guilford Press, New York, 622 pp.
- Carnec, C., C. King, D. Massonnet, and T. Rabaute. 1996a. SAR Interferometry for Monitoring Land Subsidence: Application to Areas of Underground Earth Resources Mapping. Abstract in *FRINGE 96: Proceedings ESA Workshop on Applications of ERS SAR Interferometry* (Zurich, Switzerland). <http://www.geo.unizh.ch/rsl/fringe96/papers/>
- Carnec, C., D. Massonnet, and C. King. 1996b. Two Examples of the Use of SAR Interferometry on Displacement-Fields of Small Spatial Extent. *Geophysical Research Letters*, vol. 23, no. 24, pp. 3579-3582.
- Curlander, J., and R. McDonough. 1991. *Synthetic Aperture Radar: Systems and Signal Processing*. John Wiley & Sons, New York, 672 pp.
- Dixon, T.H., ed. 1995. *SAR Interferometry and Surface Change Detection: Report of a Workshop* (Boulder, CO, Feb. 3-4, 1994). Jet Propulsion Laboratory, California Institute of Technology, under contract with National Aeronautics and Space Administration. <http://southport.jpl.nasa.gov/scienceapps/dixon/>
- Fruneau, B., and J. Achache. 1996. Satellite Monitoring of Landslides Using SAR Interferometry. *News Journal, International Society for Rock Mechanics*, vol. 3, no. 3, pp. 10-13.
- Fukuzono, T. 1990. Recent Studies on Time Prediction of Slope Failure. *Landslide News*, no. 4, pp. 9-12.
- Lundgreen, R.B., D.G. Thompson, D.V. Arnold, D.G. Long, and G.F. Miner. 2000. Initial Results of a Low-Cost SAR: YINSAR. *Proceedings of the International Geoscience and Remote Sensing Symposium* (Honolulu, HI, 24-28 July 2000). Pp. 3045-3047.
- Malassingne, C., F. Lemaître, P. Briole, and O. Pascal. 2001. Potential of Ground Based Radar for the Monitoring of Deformation of Volcanoes. *Geophysical Research Letters*, vol. 28, no. 5, pp. 851-854.
- Martinez, A., and A.P. Byrnes. 2001. Modeling Dielectric-Constant Values on Geologic Materials: An Aid to Ground-Penetrating Radar Data Collection and Interpretation. *Current Research in Earth Sciences*, Bull. 247, Part 1, pp. 1-16.
- Massonnet, D. 1997. Satellite Radar Interferometry. *Scientific American*, vol. 276, no. 2, pp. 32-39. <http://www.sciam.com/0297issue/0297massonnet.html>

- Massonnet, D., K. Feigl, M. Rossi, and F. Adragna. 1994. Radar Interferometric Mapping of Deformation in the Year after the Lander's Earthquake. *Nature*, vol. 369, pp. 227-230.
- Massonnet, D., M. Rossi, C. Carmona, F. Adragna, G. Peltzer, K. Feigl, and T. Rabaute. 1993. The Displacement Field of the Lander's Earthquake Mapped by Radar Interferometry. *Nature*, vol. 364, pp. 138-142.
- McHugh, E., and J. Girard. 2002. Evaluating Techniques for Monitoring Rock Falls and Slope Stability. *Proceedings, 21st International Conference on Ground Control in Mining*, S.S. Peng, C. Mark, A.W. Khair, and K. Heasley, eds (Morgantown, WV, 6-8 Aug., 2002). Dept. of Mining Engineering, West Virginia University, Morgantown, WV, pp. 335-343.
- McHugh, E.L., J.M. Girard, and L.J. Denes. 2001. Simplified Hyperspectral Imaging for Improved Geologic Mapping of Mine Slopes. *Proceedings of the Third International Conference on Intelligent Processing and Manufacturing of Materials*, J.A. Meech, S.M. Viega, S.R. LeClair, and J.F. Maquire, eds. (Vancouver, Canada, 29 July-2 Aug., 2001). CD ROM.
- Mine Safety and Health Administration. 2002. Fatal Machinery Accident, Cantera Master Aggregates, Arenales Bajo, Isabella, Puerto Rico, November 13, 2002. Fatal Investigation Report. <http://www.msha.gov/FATALS/2002/FAB02m38.HTM>
- Moore, R.K. 1990. Ground Echo. Ch. in *Radar Handbook*, ed. by M.I. Skolnik. McGraw-Hill, New York, pp. 12.1-12.54.
- Peake, W.H., and T.L. Oliver. 1971. The Response of Terrestrial Surfaces at Microwave Frequencies. 2440-7, Technical Report AFAL-TR-70-301. Electroscience Laboratory, Ohio State University, Columbus, OH.
- Reeves, B., D. Noon, G. Stickley, and D. Longstaff. 1997. Monitoring Rock Slope Deformation by Radar Interferometry. *Proceedings of the Workshop on Applications of Radio Science WARS'97*, A. Kulesa, ed. Australian Academy of Science, Canberra, Australia, pp. 119-123.
- Richards, J.A., and X. Jia. 1999. *Remote Sensing Digital Image Analysis*. Springer-Verlag, Berlin, 363 pp.
- Robertson, A.E. 1998. Multi-Baseline Interferometric SAR for Iterative Height Estimation. Master's thesis, Brigham Young University, Provo, UT, 140 pp.
- Schaber, G.G., J.F. McCauley, and C.S. Breed. 1997. The Use of Multifrequency and Polarimetric SIR-C/X-SAR Data in Geologic Studies of Bir Safsaf, Egypt. *Remote Sensing Environment*, vol. 59, pp. 337-363.
- Skolnik, M.I. 1990. An Introduction to Radar. Ch. in *Radar Handbook*, ed. by M.I. Skolnik. McGraw-Hill, New York, pp. 1.1-1.21.
- Stow, R. 1996. Application of SAR Interferometry to the Imaging and Measurement of Neotectonic Movement Applied to Mining and Other Subsidence/Downwarp Modeling. Abstract in *FRINGE 96: Proceedings ESA Workshop on Applications of ERS SAR Interferometry* (Zurich, Switzerland). <http://www.geo.unizh.ch/rsl/fringe96/papers/>
- Tarchi, D. N. Casagli, R. Fanti, D.D. Leva, G. Luzi, A. Pasuto, M. Pieraccini, and S. Silvano. 2003. Landslide Monitoring by Using Ground-Based SAR Interferometry: An Example of Application to the Tessina Landslide in Italy. *Engineering Geology*, vol. 68, nos. 1-2, pp. 15-30.
- Thompson, D.G. 2001. Innovative Radar Interferometry. Ph.D. dissertation, Brigham Young University, Provo, UT, 188 pp.
- Thompson, D.G., D. Arnold, D. Long, G.F. Miner, M.A. Jensen, T.W. Karlinsey, A.E. Robertson, and J.S. Bates. 1998. YINSAR: A Compact, Low-Cost Interferometric Synthetic Aperture Radar. *Proceedings of the 1998 International Geoscience and Remote Sensing Symposium* (Seattle, WA). Pp. 1920-1922.

Toomay, J.C. 1989. *Radar Principles for the Non-Specialist*. Van Nostrand Reinhold, New York, 205 pp.

University of Queensland. 2002. Slope Stability Radar Goes Commercial. On-Line News. News release, 26 June, 2002. <http://www.uq.edu.au/news/index.phtml?article=3279>

U.S. Department of Commerce. 2003. United States Frequency Allocations, the Radio Spectrum (chart). National Telecommunications and Information Administration, Office of Spectrum Management, October 2003. Available at <http://www.ntia.doc.gov/osmhome/allochrt.pdf>

Voight, B. 1989. A Relation to Describe Rate-Dependent Material Failure. *Science*, vol. 243, pp. 200-203.

Waite, J.L. 2000. Detecting Track Hazards Using an Interferometric Radar. Master's thesis, Brigham Young University, Provo, UT, 100 pp.

Zebker, H.A., and R.M. Goldstein. 1986. Topographic Mapping from Interferometric SAR Observations. *Journal of Geophysical Research*, vol. 91, no. B5, pp. 4993-4999.

Zebker, H.A., S.N. Madsen, J. Martin, K. Wheeler, T. Miller, Y-L Lou, G. Alberti, S. Vetrella, and A. Cucci. 1992. The TOPSAR Interferometric Radar Mapping Instrument. *IEEE Transactions on Geoscience and Remote Sensing*, vol. 30, no. 5, pp. 933-940.

APPENDIX A: THE SCIENCE OF RADAR

RADAR EQUATION

The radar equation (Skolnik, 1990, p. 1.6) can be written as

$$P_r = \frac{P_t G_t}{4\pi R^2} \sigma_{rt} \frac{A_r}{4\pi R^2} \quad (\text{A1})$$

where P_r = received power at polarization r ,
 P_t = transmitted power at polarization t ,
 G_t = antenna gain in direction of target at polarization t ,
 R = distance between radar and target,
 A_r = effective receiving area of receiving antenna aperture at polarization r ,
and σ_{rt} = radar cross-section or the area intercepting that amount of power of polarization t , which, when scattered isotropically, produces an echo at polarization r equal to that observed from the target.

The radar equation assumes that the transmitting and receiving antennas are at the same location. A radar beam illuminates an area of the surface that is larger than the ground resolution cell. It is useful to define an average differential, or radar cross-section per unit area, and to consider the average return power. The total average return power is found by integrating the radar return from each differential area over the entire illuminated area as follows:

$$P_{ar} = \int_{A_o} \frac{P_t G_t}{4\pi R^2} \sigma_{rt}^o \frac{A_r}{4\pi R^2} ds \quad (\text{A2})$$

where P_{ar} = total average return power,
 s = surface integral taken over the irradiated area A_o ,
and σ_{rt}^o = scattering coefficient.

The effective size of the antenna aperture is related to the antenna gain by

$$A_r = \frac{G_r \lambda^2}{4\pi} \quad (\text{A3})$$

where λ = wavelength.

Therefore,

$$P_{ar} = \frac{\lambda^2}{(4\pi)^3} \int_{A_o} \frac{P_t G_t G_r}{R^4} \sigma_{rt}^o ds. \quad (\text{A4})$$

All parameters of the radar equation (P_t , G , λ) are fixed by the operator, and R is known by the location of the radar relative to the target. The scattering coefficient is the only variable in the radar equation that governs the average return power strength. In addition to the radar parameters (P_t , G , λ , R), the scattering coefficient is also influenced by surface and volume parameters that include slope aspect relative to the radar beam, surface roughness, volume scattering, dielectric constant, depression angle, and polarization.

Pulse repetition frequency largely determines the maximum range of the radar set. If the period between successive pulses is too short, an echo from a distant target may return after the transmitter has emitted another pulse. This would

make it impossible to tell whether the observed pulse is the echo of the pulse just transmitted or the echo of the preceding pulse. This produces a situation referred to as “range ambiguity.” The maximum unambiguous range is the longest range to which a transmitted pulse can travel and return to the radar before the next pulse is transmitted.

SCATTERING MECHANISMS

The radar return from natural terrains involves both surface- and volume-scattering mechanisms. The return for snow-covered ground, for example, may include surface scattering from air-snow and snow-ground interfaces and volume scattering from the interior of the snow layer. Similar statements can be made for vegetated terrains and heterogeneous ground surfaces.

Ground surfaces can be modeled mathematically in terms of facets, spheres, cylinders, and dihedral and trihedral corner reflectors. Surface-scattering mechanisms arising from these models have been applied to three basic types of surfaces:

1. Surfaces with horizontal roughness scales greater than the incident radar wavelength,
2. Surfaces with slopes and roughness scales that are small compared with the incident wavelength, and
3. Some combination of the above mechanisms.

Volume-scattering mechanisms have been studied for two basic types of heterogeneous media: continuous heterogeneous media and homogeneous media with discrete scatterers embedded (Moore, 1990; Toomay, 1989).

Some general conclusions emerge from modeling studies. For surface scattering with incidence angles less than 30° , the expected interaction mechanism is quasi-specular reflection or diffraction from locally smooth facets that are larger than the incident radar wavelength. For incidence angles in the 30° to 80° range, any significant radar return is likely to be in the form of Bragg scattering, where roughness scales with a horizontal dimension l satisfies the relationship

$$2l \sin \theta = \lambda . \tag{A5}$$

Cross-polarized surface backscattering in the range $0^\circ \leq \theta \leq 80^\circ$ arises from scattering by multiple surfaces. The cross-polarized return is usually more than 10 db lower than the like-polarized return from the same surface.

Volume scattering from a weakly heterogeneous medium or a medium with sparsely distributed scatterers is likely to produce a polarized radar return from a single-scattering process; cross-polarized returns arise from a second-bounce mechanism. The cross-polarized return is usually more than 15 db lower than the like-polarized return. In strongly heterogeneous media, multiple scattering effects become important, producing cross-polarized signals raised to within 10 db of the like-polarized return from the same target. Multiple scattering is much more important in producing a cross-polarized component than in producing a like-polarized component.

INFLUENCES ON RADAR RETURN

Factors that influence the strength and character of return radar signals fall into two categories: system parameters and target parameters. System parameters include radar polarization, look direction, resolution cell size, wavelength, and depression angle. Target parameters include the complex dielectric constant, surface roughness, and surface cover. All of these factors are somewhat interdependent, and certain tradeoffs may be necessary to achieve the best possible radar images.

System Parameters

Polarization

Although early imaging radars used circular polarization, most imaging radars transmit electromagnetic energy with the electrical vector in the horizontal plane and can receive return signals in either the horizontal (HH or like-polarized) or vertical (HV or cross-polarized) plane. Differences in tonality between like- and cross-polarized returns in radar imagery can be used to differentiate geologic and geographic features.

Four mechanisms are known to cause cross-polarized radar returns (Campbell, 1996):

1. Quasi-specular reflection,
2. Multiple scattering as a result of surface roughness,
3. Multiple volume scattering due to heterogeneities, especially those embedded within a skin depth of a target surface, and
4. Physical or geometric anisotropic properties of a target.

The first three of these are commonly encountered in remote-sensing applications. Quasi-specular reflection from smoothly undulating surfaces predicts essentially no cross-polarized return at near-vertical incidence angles and increasing levels of cross-polarization at larger incidence angles. The cross-polarized component is weak compared to the like-polarized return. Cross-polarized returns due to multiple reflections from rough surfaces and from volume scattering predict fairly uniform returns at all incidence angles except near-grazing. Multiple volume scattering produces stronger cross-polarized returns than scattering due to surface roughness. Multiple volume scattering from vegetation is also a major cause of cross-polarization. Returns from bare ground have little or no cross-polarized component. The difference in strength of returns from like- and cross-polarized signals remains fairly constant as incidence angles increase to near-grazing.

Look Direction

Look direction, the direction of the transmitted radar beam, can be crucial to the quality of a radar image. Look direction is generally perpendicular to the direction of movement of the radar platform and is commonly oriented perpendicular to the structural or topographic “grain” of the terrain being observed. This orientation achieves maximum backscatter from features such as mountain slopes and stream banks. Stream channels that are perpendicular to the look direction stand out in sharp relief in radar images with the near bank in radar shadow and the opposite bank brightly illuminated. Although streams parallel to the look direction may disappear in a radar image, for interferometry, it is sometimes useful to look with the grain to avoid layover and shadows.

Resolution Cell

The resolution cell is the region on the ground contributing to the return signal that generates a point on the image at a particular instant. The resolution cell is determined by the half-power angular width of the antenna pattern, the time interval of the transmitted pulse, and, for synthetic aperture radar, the bandwidth of the Doppler filter. All scatterers in a resolution cell contribute collectively to the gray tone of a point on an image, but not all scatterers are identifiable unless there is significant contrast with the background gray level. A bright roof facing the radar antenna might be identifiable even if it is smaller than the resolution cell.

The characteristic grainy appearance of a radar image results from destructive and constructive interference among the reflections from individual surface scattering centers within a resolution cell. These interference effects are random due to slight differences in the direction and angle of view even in areas with relatively uniform properties, causing brightness variations in adjacent pixels known as speckle. Speckle can be reduced by averaging multiple looks at a piece of ground during image acquisition, or by applying a median filter during image processing. However, this filtering will result in a loss of spatial resolution in the image.

The ground-resolution cell is determined by specific characteristics of the radar system. These include depression angle γ , pulse length τ , wavelength λ , antenna length D , and slant range distance S . The size of the resolution cell is determined by range resolution R_r , or resolution in the look direction, and azimuth resolution R_a , or resolution in the direction of the flight line.

Range resolution is determined by depression angle and pulse length and is theoretically equal to one-half the pulse length. Range resolution is given by

$$R_r = \frac{\tau}{2 \cos \gamma}. \quad (\text{A6})$$

Because the radar measures the range distance to features in slant range rather than true horizontal distance along the ground, in a slant-range image, features in the near range would appear compressed relative to the far range. The cosine of the depression angle converts slant range to ground range resolution. Equation A6 shows the inverse relationship between depression angle and ground range resolution; as the angle increases from 0° to 90° , the cosine of the angle decreases from 1 to 0. Therefore as the depression angle increases (nearer range) the ground resolution cell gets larger, resulting in a decrease in spatial detail.

Shortening the pulse length will achieve higher range resolution, but the energy in each transmitted pulse will be reduced. A longer pulse will transmit more power to the target and in turn more power will be reflected, resulting in increased target information and greater reliability. The trade-off between range resolution and pulse length can be partly resolved using frequency modulation, or “chirp.”

Instead of a short pulse, a longer pulse can be used with an upward or downward linear sweep of frequencies encoded within the transmitted radar pulse. The return signal is stored in memory and processed by Fourier transformation together with a reference wave. The result is a unique frequency that places the reflector at a point within the radar pulse.

Resolution in the azimuth direction is determined by the width of the radar footprint on the ground. To be resolved, two objects must be separated by a distance greater than the beam width on the ground. The trace of the radar beam on the ground is fan shaped, so azimuth resolution in the near range will be better than in the far range. The angular beam width is proportional to the radar wavelength, so resolution is better at shorter wavelengths than longer. The angular beam width is also inversely proportional to the antenna length D . A long antenna creates a narrow beam width, but there is a practical limit to the antenna length that can be carried by an aircraft or an orbital platform. For a real-aperture radar, azimuth resolution is given by

$$R_a = \frac{1}{2} \frac{S\lambda}{D}. \quad (\text{A7})$$

Synthetic aperture radar resolves the difference in azimuth resolution between the near and far range by tracking the apparent Doppler frequency shift of objects as the radar beam sweeps across them. Any particular target is illuminated by the radar beam for a finite time period T and

$$T = L/v \quad (\text{A8})$$

where v = velocity of platform
and L = azimuthal dimension of the radar footprint, which can be written as

$$L = \frac{S\lambda}{D}. \quad (\text{A9})$$

During time period T the apparent motion of a target through the radar beam yields a time-dependent Doppler shift in the frequency of the return pulse. This Doppler phase history can then be used to distinguish between targets within the same footprint through a process of Fourier analysis and matched filter processing. Thus the target's illumination is equivalent to that from a synthetic aperture of length vT , which is simply L . The resulting azimuthal resolution can be obtained from equation A7 in which D is replaced by L .

$$R_a = \frac{1}{2} \frac{S\lambda}{L} = \frac{1}{2} S\lambda \frac{D}{S\lambda} = \frac{D}{2}. \quad (\text{A10})$$

The azimuthal resolution is therefore independent of platform height and depends only on the size of the antenna.

Wavelength

The wavelength of incident radiation affects the scattered signal by (1) defining the effective surface roughness and (2) determining the depth of penetration and consequent volume effects of the ground surface. The relation between wavelength and surface roughness is described in the section on "Target Parameters."

The depth of surface penetration depends in part on the wavelength of the incident radiation. "Skin depth" defines the depth below the surface at which the amplitude of the incident radiation is reduced to 37% of the surface value. This quantity is determined by

$$\delta = \left(\frac{\lambda}{\pi \zeta \eta} \right)^{\frac{1}{2}} \quad (\text{A11})$$

where δ = skin depth,
 λ = wavelength,
 ζ = conductivity,

$$\eta = \left(\frac{\mu}{\varepsilon} \right)^{\frac{1}{2}},$$

and μ = permeability of terrain,
 ε = permittivity of terrain.

Permittivity is strongly dependent on soil moisture. Moist soils allow very little penetration of incident radiation, while very dry and permeable soils, such as aeolian sands in hyperarid environments, might allow penetration of L-band radiation to several meters.

Depression Angle

Depression angle is usually defined as the angle between the horizontal plane at the antenna and the line of sight to an illuminated spot on the ground. The average depression angle refers to the line that marks the midpoint of the radar beam in the range direction, while the minimum and maximum depression angles refer to the far-range and near-range lines of sight. The depression angle can have a significant effect on the radar image. Too shallow an angle results in excessive radar shadow on the back side of mountains and ridges and minimal backscatter; too steep an angle causes foreshortening of slopes facing the antenna or layover of steep slopes. Layover occurs where the radar pulse intersects the top of a slope before the bottom, causing the slope to appear to lean toward the antenna in the image. Most imaging radars employ a depression angle of 30° to 40° for terrestrial observation; scatterometers operate over a broader range (30° to 80°) of depression angles.

Target Parameters

Relative Complex Dielectric Constant

The relative complex dielectric constant ε is an electrical property of matter that can strongly affect radar returns. It is commonly written as

$$\varepsilon = \varepsilon' - j\varepsilon'' \quad (\text{A12})$$

where ε' = the real part, often referred to as the relative permittivity,
 and ε'' = an imaginary part, also known as the loss factor or conductivity.

The term relative means that ε is normalized to the permittivity of free space ε_0 . Most surface materials have dielectric constants between about 3 and 8 (Martinez and Byrnes, 2001). Water has a dielectric constant of 80. Moisture in rocks and soils can raise their dielectric constants to about 20. Increasing the dielectric constant of surface materials due to water content increases the backscatter coefficient, which in turn increases the tonality of the radar image.

The strong polarity of water molecules accounts for its high dielectric constant. Water molecules in soils and vegetation oscillate in harmony with the electrical vector of radar waves over a wide range of radar frequencies, greatly enhancing the strength of the return signal. Virtually no energy penetrates the surface if even small amounts of water are present. Conversely, radar energy can penetrate as much as 2 m into hyperarid soils from space-borne platforms, as has been demonstrated in the aeolian sands of the Sahel in northern Africa (Schaber and others, 1997).

Surface Roughness

Surface roughness is the terrain property that has the greatest influence on the strength of radar returns. Measured in centimeters, roughness refers to textural features that are comparable in size to radar wavelengths. The average height of surface irregularities can be taken as a measure of roughness.

Three categories of roughness are commonly defined. Smooth surfaces are those in which radar energy is reflected forward according to Snell's law (specular reflection) with virtually no backscatter toward the receiving antenna. Rough surfaces result in diffuse, hemispherical scattering in all directions of radar energy with a significant return to the antenna. An intermediate category is a mixture of specular and hemispherical reflection.

Criteria for roughness depends on the wavelength of the incident radar beam and its depression angle. The Rayleigh criterion considers a surface to be smooth if

$$h < \frac{\lambda}{8 \sin \gamma} \quad (\text{A13})$$

where h = vertical relief in centimeters,
 λ = radar wavelength in centimeters,
 and γ = depression angle of incident radar.

Peake and Oliver (1971) modified the Rayleigh criterion, defining a smooth criterion as

$$h < \frac{\lambda}{25 \sin \gamma} \quad (\text{A14})$$

and a rough criterion as

$$h < \frac{\lambda}{4.4 \sin \gamma}. \quad (\text{A15})$$

Surface Cover

The backscattering coefficient of bare soil is influenced by soil moisture, random roughness, periodic surface patterns (e.g., row tillage), and soil texture. Soil moisture and soil texture are governed chiefly by dielectric properties, or water content. Backscattering properties due to roughness and surface patterns depend in part on the wavelength of incident radiation. A soil may appear rough at short wavelengths and smooth at longer wavelengths.

Vegetation may be viewed as a mixture of leaves, fruit, branches, and stalks embedded in air. Returns from deciduous leaves may dominate the total radar return, particularly in the spring when their water content is high. Radar returns from vegetation are also dependent on wavelength. Short wavelengths will interact more with tree canopies, leading to strong volume scattering from foliage. Long wavelengths tend to penetrate canopies and interact with the ground surface.

APPENDIX B: DATA TABLES ON FIELD EXPERIMENTS USING RADAR TO DETECT MINING HAZARDS

Table B1.—Phase data for a segment of test 4; phase = $(Dv-127)/41$ and $\Delta\text{Phase} = \Delta Dv/41$

Time, sec	Pixel location		Data value, Dv	Phase, Radians	Phase change		Displacement, cm
	x	y			ΔDv	$\Delta\text{Radians}$	
13.03	459	310	64	-1.54			
13.09	459	311	14	-2.76	-50	-1.22	-0.6
13.14	459	312	17	-2.68	3	0.07	0.0
13.19	459	313	15	-2.73	-2	-0.05	0.0
13.24	459	314	16	-2.71	1	0.02	0.0
13.30	459	315	37	-2.20	21	0.51	0.2
13.35	459	316	18	-2.66	-19	-0.46	-0.2
13.40	459	317	17	-2.68	-1	-0.02	0.0
13.46	459	318	19	-2.63	2	0.05	0.0
13.51	459	319	26	-2.46	7	0.17	0.1
13.56	459	320	18	-2.66	-8	-0.20	-0.1
13.62	459	321	16	-2.71	-2	-0.05	0.0
13.67	459	322	20	-2.61	4	0.10	0.0
13.72	459	323	20	-2.61	0	0.00	0.0
13.78	459	324	24	-2.51	4	0.10	0.0
13.83	459	325	29	-2.39	5	0.12	0.1
13.88	459	326	31	-2.34	2	0.05	0.0
13.94	459	327	21	-2.59	-10	-0.24	-0.1
13.99	459	328	28	-2.41	7	0.17	0.1
14.04	459	329	26	-2.46	-2	-0.05	0.0
14.10	459	330	29	-2.39	3	0.07	0.0
14.15	459	331	22	-2.56	-7	-0.17	-0.1
14.20	459	332	33	-2.29	11	0.27	0.1
14.26	459	333	28	-2.41	-5	-0.12	-0.1
14.31	459	334	25	-2.49	-3	-0.07	0.0
14.36	459	335	26	-2.46	1	0.02	0.0
14.42	459	336	27	-2.44	1	0.02	0.0
14.47	459	337	20	-2.61	-7	-0.17	-0.1
14.52	459	338	27	-2.44	7	0.17	0.1
14.57	459	339	27	-2.44	0	0.00	0.0
14.63	459	340	19	-2.63	-8	-0.20	-0.1
14.68	459	341	20	-2.61	1	0.02	0.0
14.73	459	342	18	-2.66	-2	-0.05	0.0
14.79	459	343	21	-2.59	3	0.07	0.0
14.84	459	344	17	-2.68	-4	-0.10	0.0
14.89	459	345	26	-2.46	9	0.22	0.1
14.95	459	346	17	-2.68	-9	-0.22	-0.1
15.00	459	347	22	-2.56	5	0.12	0.1
15.05	459	348	24	-2.51	2	0.05	0.0
15.11	459	349	28	-2.41	4	0.10	0.0
15.16	459	350	30	-2.37	2	0.05	0.0

Table B1.—Phase data for a segment of test 4; phase = (Dv-127)/41 and Δ Phase = Δ Dv/41

Time, sec	Pixel location		Data value, Dv	Phase, Radians	Phase change		Displacement, cm
	x	y			Δ Dv	Δ Radians	
15.21	459	351	20	-2.61	-10	-0.24	-0.1
15.27	459	352	31	-2.34	11	0.27	0.1
15.32	459	353	21	-2.59	-10	-0.24	-0.1
15.37	459	354	25	-2.49	4	0.10	0.0
15.43	459	355	21	-2.59	-4	-0.10	0.0
15.48	459	356	24	-2.51	3	0.07	0.0
15.53	459	357	51	-1.85	27	0.66	0.3
15.59	459	358	21	-2.59	-30	-0.73	-0.3
15.64	459	359	21	-2.59	0	0.00	0.0
15.69	459	360	20	-2.61	-1	-0.02	0.0
15.74	459	361	27	-2.44	7	0.17	0.1
15.80	459	362	24	-2.51	-3	-0.07	0.0
15.85	459	363	26	-2.46	2	0.05	0.0
15.90	459	364	22	-2.56	-4	-0.10	0.0
15.96	459	365	27	-2.44	5	0.12	0.1
16.01	459	366	23	-2.54	-4	-0.10	0.0
16.06	459	367	19	-2.63	-4	-0.10	0.0
16.12	459	368	27	-2.44	8	0.20	0.1
16.17	459	369	19	-2.63	-8	-0.20	-0.1
16.22	459	370	30	-2.37	11	0.27	0.1
16.28	459	371	25	-2.49	-5	-0.12	-0.1
16.33	459	372	31	-2.34	6	0.15	0.1
16.38	459	373	29	-2.39	-2	-0.05	0.0
16.44	459	374	29	-2.39	0	0.00	0.0
16.49	459	375	28	-2.41	-1	-0.02	0.0
16.54	459	376	36	-2.22	8	0.20	0.1
16.60	459	377	23	-2.54	-13	-0.32	-0.2
16.65	459	378	29	-2.39	6	0.15	0.1
16.70	459	379	24	-2.51	-5	-0.12	-0.1
16.76	459	380	26	-2.46	2	0.05	0.0
16.81	459	381	28	-2.41	2	0.05	0.0
16.86	459	382	25	-2.49	-3	-0.07	0.0
16.92	459	383	27	-2.44	2	0.05	0.0
16.97	459	384	28	-2.41	1	0.02	0.0
17.02	459	385	29	-2.39	1	0.02	0.0
17.07	459	386	30	-2.37	1	0.02	0.0
17.13	459	387	28	-2.41	-2	-0.05	0.0
17.18	459	388	23	-2.54	-5	-0.12	-0.1
17.23	459	389	30	-2.37	7	0.17	0.1
17.29	459	390	30	-2.37	0	0.00	0.0
17.34	459	391	31	-2.34	1	0.02	0.0
17.39	459	392	28	-2.41	-3	-0.07	0.0
17.45	459	393	25	-2.49	-3	-0.07	0.0
17.50	459	394	40	-2.12	15	0.37	0.2
17.55	459	395	34	-2.27	-6	-0.15	-0.1
17.61	459	396	19	-2.63	-15	-0.37	-0.2

Table B1.—Phase data for a segment of test 4; phase = (Dv-127)/41 and Δ Phase = Δ Dv/41

Time, sec	Pixel location		Data value, Dv	Phase, Radians	Phase change		Displacement, cm
	x	y			Δ Dv	Δ Radians	
17.66	459	397	37	-2.20	18	0.44	0.2
17.71	459	398	52	-1.83	15	0.37	0.2
17.77	459	399	35	-2.24	-17	-0.41	-0.2
17.82	459	400	15	-2.73	-20	-0.49	-0.2
17.87	459	401	42	-2.07	27	0.66	0.3
17.93	459	402	10	-2.85	-32	-0.78	-0.4
17.98	459	403	13	-2.78	3	0.07	0.0
18.03	459	404	20	-2.61	7	0.17	0.1
18.09	459	405	126	-0.02	106	2.59	1.2
18.14	459	406	45	-2.00	-81	-1.98	-0.9
18.19	459	407	31	-2.34	-14	-0.34	-0.2
18.24	459	408	223	2.34	192	4.68	2.2
18.30	459	409	177	1.22	-46	-1.12	-0.5
18.35	459	410	9	-2.88	-168	-4.10	-1.976
18.40	459	411	53	-1.80	44	1.07	0.5
18.46	459	412	14	-2.76	-39	-0.95	-0.5
18.51	459	413	79	-1.17	65	1.59	0.8
18.56	459	414	59	-1.66	-20	-0.49	-0.2
18.62	459	415	35	-2.24	-24	-0.59	-0.3
18.67	459	416	79	-1.17	44	1.07	0.5
18.72	459	417	86	-1.00	7	0.17	0.1
18.78	459	418	77	-1.22	-9	-0.22	-0.1
18.83	459	419	67	-1.46	-10	-0.24	-0.1
18.88	459	420	101	-0.63	34	0.83	0.4
18.94	459	421	54	-1.78	-47	-1.15	-0.5
18.99	459	422	135	0.20	81	1.98	0.9
19.04	459	423	44	-2.02	-91	-2.22	-1.1
19.10	459	424	53	-1.80	9	0.22	0.1
19.15	459	425	32	-2.32	-21	-0.51	-0.2
19.20	459	426	51	-1.85	19	0.46	0.2
19.26	459	427	132	0.12	81	1.98	0.9
19.31	459	428	97	-0.73	-35	-0.85	-0.4
19.36	459	429	57	-1.71	-40	-0.98	-0.5
19.42	459	430	115	-0.29	58	1.41	0.7
19.47	459	431	20	-2.61	-95	-2.32	-1.1
19.52	459	432	129	0.05	109	2.66	1.3
19.57	459	433	4	-3.00	-125	-3.05	-1.5
19.63	459	434	230	2.51	226	5.51	2.6
19.68	459	435	30	-2.37	-200	-4.88	-2.3
19.73	459	436	101	-0.63	71	1.73	0.8
19.79	459	437	26	-2.46	-75	-1.83	-0.9
19.84	459	438	177	1.22	151	3.68	1.8
19.89	459	439	253	3.07	76	1.85	0.9
19.95	459	440	28	-2.41	-225	-5.49	-2.6
20.00	459	441	28	-2.41	0	0.00	0.0
20.05	459	442	240	2.76	212	5.17	2.5

Table B1.—Phase data for a segment of test 4; phase = (Dv-127)/41 and Δ Phase = Δ Dv/41

Time, sec	Pixel location		Data value, Dv	Phase, Radians	Phase change		Displacement, cm
	x	y			Δ Dv	Δ Radians	
20.11	459	443	77	-1.22	-163	-3.98	-1.9
20.16	459	444	10	-2.85	-67	-1.63	-0.8
20.21	459	445	17	-2.68	7	0.17	0.1
20.27	459	446	27	-2.44	10	0.24	0.1
20.32	459	447	222	2.32	195	4.76	2.3
20.37	459	448	230	2.51	8	0.20	0.1
20.43	459	449	16	-2.71	-214	-5.22	-2.5
20.48	459	450	15	-2.73	-1	-0.02	0.0
20.53	459	451	11	-2.83	-4	-0.10	0.0
20.59	459	452	22	-2.56	11	0.27	0.1
20.64	459	453	7	-2.93	-15	-0.37	-0.2
20.69	459	454	28	-2.41	21	0.51	0.2
20.74	459	455	127	0.00	99	2.41	1.2
20.80	459	456	56	-1.73	-71	-1.73	-0.8
20.85	459	457	124	-0.07	68	1.66	0.8
20.90	459	458	243	2.83	119	2.90	1.4
20.96	459	459	128	0.02	-115	-2.80	-1.3
21.01	459	460	47	-1.95	-81	-1.98	-0.9
21.06	459	461	246	2.90	199	4.85	2.3
21.12	459	462	18	-2.66	-228	-5.56	-2.7
21.17	459	463	172	1.10	154	3.76	1.8
21.22	459	464	176	1.20	4	0.10	0.0
21.28	459	465	6	-2.95	-170	-4.15	-2.0
21.33	459	466	127	0.00	121	2.95	1.4
21.38	459	467	111	-0.39	-16	-0.39	-0.2
21.44	459	468	210	2.02	99	2.41	1.2
21.49	459	469	10	-2.85	-200	-4.88	-2.3
21.54	459	470	231	2.54	221	5.39	2.6
21.60	459	471	110	-0.41	-121	-2.95	-1.4
21.65	459	472	180	1.29	70	1.71	0.8
21.70	459	473	7	-2.93	-173	-4.22	-2.0
21.76	459	474	132	0.12	125	3.05	1.5
21.81	459	475	53	-1.80	-79	-1.93	-0.9
21.86	459	476	37	-2.20	-16	-0.39	-0.2
21.91	459	477	92	-0.85	55	1.34	0.6
21.97	459	478	42	-2.07	-50	-1.22	-0.6
22.02	459	479	46	-1.98	4	0.10	0.0
22.07	459	480	95	-0.78	49	1.20	0.6
22.13	459	481	224	2.37	129	3.15	1.5
22.18	459	482	136	0.22	-88	-2.15	-1.0
22.23	459	483	240	2.76	104	2.54	1.2
22.29	459	484	220	2.27	-20	-0.49	-0.2
22.34	459	485	221	2.29	1	0.02	0.0
22.39	459	486	130	0.07	-91	-2.22	-1.1
22.45	459	487	107	-0.49	-23	-0.56	-0.3
22.50	459	488	237	2.68	130	3.17	1.5

Table B1.—Phase data for a segment of test 4; phase = (Dv-127)/41 and Δ Phase = Δ Dv/41

Time, sec	Pixel location		Data value, Dv	Phase, Radians	Phase change		Displacement, cm
	x	y			Δ Dv	Δ Radians	
22.55	459	489	57	-1.71	-180	-4.39	-2.1
22.61	459	490	194	1.63	137	3.34	1.6
22.66	459	491	38	-2.17	-156	-3.80	-1.8
22.71	459	492	224	2.37	186	4.54	2.2
22.77	459	493	30	-2.37	-194	-4.73	-2.3
22.82	459	494	226	2.41	196	4.78	2.3
22.87	459	495	247	2.93	21	0.51	0.2
22.93	459	496	103	-0.59	-144	-3.51	-1.7
22.98	459	497	14	-2.76	-89	-2.17	-1.0
23.03	459	498	43	-2.05	29	0.71	0.3
23.09	459	499	22	-2.56	-21	-0.51	-0.2
23.14	459	500	60	-1.63	38	0.93	0.4
23.19	459	501	77	-1.22	17	0.41	0.2
23.24	459	502	60	-1.63	-17	-0.41	-0.2
23.30	459	503	26	-2.46	-34	-0.83	-0.4
23.35	459	504	89	-0.93	63	1.54	0.7
23.40	459	505	41	-2.10	-48	-1.17	-0.6
23.46	459	506	37	-2.20	-4	-0.10	0.0
23.51	459	507	44	-2.02	7	0.17	0.1
23.56	459	508	31	-2.34	-13	-0.32	-0.2
23.62	459	509	70	-1.39	39	0.95	0.5
23.67	459	510	33	-2.29	-37	-0.90	-0.4
23.72	459	511	37	-2.20	4	0.10	0.0
23.78	459	512	39	-2.15	2	0.05	0.0
23.83	459	513	18	-2.66	-21	-0.51	-0.2
23.88	459	514	36	-2.22	18	0.44	0.2
23.94	459	515	35	-2.24	-1	-0.02	0.0
23.99	459	516	22	-2.56	-13	-0.32	-0.2
24.04	459	517	10	-2.85	-12	-0.29	-0.1
24.10	459	518	17	-2.68	7	0.17	0.1
24.15	459	519	21	-2.59	4	0.10	0.0
24.20	459	520	21	-2.59	0	0.00	0.0
24.26	459	521	24	-2.51	3	0.07	0.0
24.31	459	522	21	-2.59	-3	-0.07	0.0
24.36	459	523	31	-2.34	10	0.24	0.1
24.41	459	524	10	-2.85	-21	-0.51	-0.2
24.47	459	525	25	-2.49	15	0.37	0.2
24.52	459	526	19	-2.63	-6	-0.15	-0.1
24.57	459	527	25	-2.49	6	0.15	0.1
24.63	459	528	27	-2.44	2	0.05	0.0
24.68	459	529	21	-2.59	-6	-0.15	-0.1
24.73	459	530	16	-2.71	-5	-0.12	-0.1
24.79	459	531	29	-2.39	13	0.32	0.2
24.84	459	532	13	-2.78	-16	-0.39	-0.2
24.89	459	533	11	-2.83	-2	-0.05	0.0
24.95	459	534	32	-2.32	21	0.51	0.2

Table B1.—Phase data for a segment of test 4; phase = (Dv-127)/41 and ΔPhase = ΔDv/41

Time, sec	Pixel location		Data value, Dv	Phase, Radians	Phase change		Displacement, cm
	x	y			ΔDv	ΔRadians	
25.00	459	535	25	-2.49	-7	-0.17	-0.1
25.05	459	536	31	-2.34	6	0.15	0.1
25.11	459	537	25	-2.49	-6	-0.15	-0.1
25.16	459	538	25	-2.49	0	0.00	0.0
25.21	459	539	23	-2.54	-2	-0.05	0.0
25.27	459	540	37	-2.20	14	0.34	0.2
25.32	459	541	20	-2.61	-17	-0.41	-0.2
25.37	459	542	39	-2.15	19	0.46	0.2
25.43	459	543	28	-2.41	-11	-0.27	-0.1
25.48	459	544	42	-2.07	14	0.34	0.2
25.53	459	545	71	-1.37	29	0.71	0.3
25.59	459	546	32	-2.32	-39	-0.95	-0.5

Table B2.—Interferogram range profiles, test 4. Phase = (mean dv-127) ÷ 41. Phase in radians.

Time, sec	Y axis	Range, meters																				
		26.4	26.9	27.5	28.2	28.8	29.3	30	30.6	31.1	31.8	32.4	32.9	33.6	34.2	34.7	35.4	36	36.5	37.2	37.8	38.5
X axis		419	423	427	432	436	440	445	449	453	458	462	466	471	475	479	484	488	492	497	501	506
		Before																				
Mean	10.00 254	131	135	185	135	109	165	121	97	60	17	56	86	127	179	197	138	120	156	202	151	112
	10.48 263	134	72	96	121	132	171	123	96	55	12	49	89	127	179	205	154	107	102	150	169	165
Phase		133	104	141	128	121	168	122	96.5	57.5	14.5	52.5	87.5	127	179	201	146	114	129	176	160	139
		0.13	-0.57	0.33	0.02	-0.16	1.00	-0.12	-0.74	-1.70	-2.74	-1.82	-0.96	0.00	1.27	1.80	0.46	-0.33	0.05	1.20	0.80	0.28
		During																				
Mean	18.19 408	153	90	102	75	89	155	129	106	51	223	214	128	149	49	98	48	41	124	133	92	132
	22.29 485	153	159	124	144	152	171	188	166	225	221	157	42	138	167	193	182	133	101	113	104	122
Phase		153	125	113	110	121	163	159	136	138	222	186	85	144	108	146	115	87	113	123	98	127
		0.63	-0.06	-0.34	-0.43	-0.16	0.88	0.77	0.22	0.27	2.32	1.43	-1.02	0.40	-0.46	0.45	-0.29	-0.98	-0.35	-0.10	-0.71	0.00
		After																				
Mean	24.15 520	127	123	126	145	86	108	133	86	86	21	48	79	107	172	83	60	72	95	107	118	101
	28.40 600	162	82	93	195	108	73	152	108	63	15	34	51	87	155	216	90	60	94	108	168	110
Phase		145	103	110	170	97	90.5	143	97	74.5	18	41	65	97	164	150	75	66	94.5	108	143	106
		0.43	-0.60	-0.43	1.05	-0.73	-0.89	0.38	-0.73	-1.28	-2.66	-2.10	-1.51	-0.73	0.89	0.55	-1.27	-1.49	-0.79	-0.48	0.39	-0.52



**Delivering on the Nation's promise:
Safety and health at work for all people
Through research and prevention**

To receive documents or more information about occupational safety and health topics,
contact NIOSH at

1-800-35-NIOSH (1-800-356-4574)

FAX: 513-533-8573

e-mail pubstaft@cdc.gov

or visit the NIOSH Web site at www.cdc.gov/niosh

SAFER • HEALTHIER • PEOPLE™

DHHS (NIOSH) Publication No. 2006-116